RESULTS OF CORRELATIONS FOR TRANSITION LOCATION ON A CLEAN-UP GLOVE INSTALLED ON AN F-14 AIRCRAFT AND DESIGN STUDIES FOR A LAMINAR GLOVE FOR THE X-29 AIRCRAFT ACCOUNTING FOR SPANWISE PRESSURE GRADIENT

56-05

19853

S. H. Goradia
Vigyan Research Incorporated
Hampton, Virginia

and

P. J. Bobbitt; H. L. Morgan; J. C. Ferris; and W. D. Harvey
NASA Langley Research Center
Hampton, Virginia

SUMMARY

Results of correlative and design studies for transition location, laminar and turbulent boundary-layer parameters, and wake drag for forward swept and aft swept wings are presented in this paper. These studies were performed with the use of newly developed, improved integral-type boundary-layer and transition-prediction methods. Theoretical predictions were compared with flight measurements at subsonic and transonic flow conditions for the variable aft swept wing F-14 aircraft for which experimental pressure distributions, transition locations, and turbulent boundary-layer velocity profiles have been measured. Flight data were available at three spanwise stations for several values of sweep, freestream unit Reynolds number, Mach numbers, and lift coefficients. Theory/experiment correlations indicate excellent agreement for both transition location and turbulent boundary-layer parameters. The results of parametric studies carried out during the design of a laminar glove for the forward swept wing X-29 aircraft are also presented. These studies included the effects of a spanwise pressure gradient on transition location and wake drag for several values of freestream Reynolds numbers at a freestream Mach number of 0.9.

INTRODUCTION

The rise in jet fuel prices during the last decade, and uncertainties of the fuel costs for the future have been the cause of continued worldwide interest in improving military and commercial aircraft fuel efficiency. Additionally, improvements in the range of military aircraft are additional factors for achieving aircraft fuel efficiency and drag reductions. The most promising aerodynamic means of achieving significant gains in aircraft fuel efficiency is to design wings that provide extensive regions of laminar flow (refs. 1 and 2). Laminarization of the boundary layer on the surface of an

aircraft wing can be accomplished by the use of concepts such as Natural Laminar Flow (NLF), Laminar Flow Control (LFC), and a combination of NLF and LFC which is referred to as Hybrid Laminar Flow Control (HLFC).

Extensive regions of laminar flow can be maintained on a wing surface with the NLF concept by suitably tailoring the spanwise and chordwise pressure gradients to limit the amplification of disturbances that trigger the transition of the laminar boundary layer to a turbulent one. Flight tests at the Dryden Flight Research Facility on a variable sweep TACT F-111 Fighter aircraft (ref. 3) with an NLF wing glove have demonstrated that natural laminar flow can be maintained over significant areas at transonic speeds. Recent flight tests of a laminar clean-up glove (a thin, smooth fiberglass coating) on an F-14 aircraft with a variable-sweep wing (ref. 4), equipped with instrumentation for the accurate determination of transition, also revealed similar phenomena. Correlative studies were performed during the present study for the F-14 aircraft laminar wing, clean-up glove using the methods of references 5 and 6 extended to account for spanwise pressure gradient effects. Results of these studies are presented in this paper in the form of theory/experiment correlations for transition location and turbulent boundary-layer parameters. In addition, comparisons of the hot-film experimental data on the F-14 aircraft's wing glove with theoretical predictions are described.

The design of either forward- or aft-swept laminar flow wings at subsonic, transonic, or supersonic speeds, using NLF, HLFC, or LFC concepts requires the use of reliable theoretical computational methods. A number of finite-difference boundary-layer methods, stability methods, and full Navier-Stokes equation solvers are available; however, these methods are not well suited for the large number of calculations required for parametric wing design and optimization studies. Several new theoretical integral-boundary-layer methods (references 5, 6, 7, and 8) have small computer execution times and are very simple to use. These codes have the capability of predicting the laminar, transitional, and separating turbulent boundary layers for applications at subsonic, transonic, and supersonic Mach numbers.

The design studies reported in this paper involve the design of an NLF glove for the forward swept X-29 wing. The methods of references 5, 6, 7, and 8 have been modified for the present theoretical investigations to allow consideration of the effects of spanwise pressure gradient. Results are presented utilizing these modified codes for various spanwise pressure gradients and a prescribed streamwise pressure distribution to determine the extent of laminar flow on the corresponding X-29 wing glove. The wing sections' upper-surface geometrical changes required to obtain the prescribed pressure distribution are also given. Furthermore, the present design-optimization studies show qualitatively the procedure for optimizing values of spanwise gradients so as to minimize the wake drag with due consideration of the effect of imbedded shocks on the boundary layer. Finally a comparison of the extent of laminar flow on "equivalent" forward-swept and aft-swept wing configurations is made.

168

NOMENCLATURE

AR	aspect ratio
ASW	aft swept wing
c	chord
C_{D_i}	induced drag coefficient $= \dfrac{C_L^2}{\pi\, AR\, e}$
$C_{D_{wake}}$	wake drag coefficient
C_p	pressure coefficient or specific heat of air at constant pressure
$C_{P_{sonic}}$	pressure coefficient corresponding to local Mach number of 1.0
ΔC_{P_1} or ΔC_{P_c}	defined in figure 18
C_{1_i}	indicator of either growth or decay of disturbance for U component of velocity in transformed plane
C_{1_r}	downstream rate of propagation of disturbance for U component of velocity in transformed plane
C_{2_i}	indicator of either growth or decay of disturbance for W component of velocity in transformed plane
C_{2_r}	spanwise rate of propagation of disturbance of W component of velocity in the transformed plane
e	wing efficiency factor for induced drag
FSW	forward swept wing
H	form factor $= \dfrac{\delta^*}{\theta}$
L, M, N K, λ	groups of dimensionless parameters in transformed planes presenting the effects of suction, pressure gradient and curvature of velocity profiles. Each symbol defined in text.
L.E.	leading edge
M	Mach number (used only with subscripts)
N.F.	transition or instability due to normal flow
P	static pressure
P_r	Prandtl number

q	dynamic head
Q_x or Q_z	dimensionless parameter representing effects of suction and pressure gradient on the shape of velocity profile in transformed plane

$$Q_x = \frac{\delta_{T,s}^2}{\nu_0} \frac{dU_e}{dX} + \frac{V_s \delta_{T,s}}{\nu_0} \;\; ; \;\; Q_z = \frac{\delta_{T,z}^2}{\nu_0} \frac{dW_e}{dZ} + \frac{V_s \delta_{T,z}}{\nu_0}$$

R_∞	freestream Reynolds number based on chord $= \dfrac{U_\infty c}{\nu_\infty}$
$R_{T,n}$	$= \dfrac{\left(\begin{matrix} Ue \\ \text{or} \\ We \end{matrix}\right) \delta_{T,n}^{**}}{\nu_m}$
R_{inst}	value of $R_{T,n}$ at neutral point
R_{tran}	value of $R_{T,n}$ at transition
s, ξ, z	curvilinear coordinates in physical plane; s is normal to local sweep lines on wing surface, ξ normal to wing surface, and z normal to s-ξ plane in spanwise direction
S.F.	transition or instability due to spanwise flow
T	temperature, ^oR
T.E.	trailing edge
u, v, w	velocity components in physical planes in s, ξ and z directions, respectively
U, V, W	velocity components in transformed planes in X, Y, and Z directions, respectively
x, y	wing section coordinates in streamwise direction
X, Y	Stewartson's transformed coordinates

$$X = \int_0^s \alpha \frac{a_e}{a_0} \frac{P_e}{P_0} ds ; \qquad Y = \frac{a_e}{a_0} \frac{\rho_e}{\rho_0} \int_0^\xi \frac{T_e}{T} d\xi$$

Ψ_1	disturbance stream function for transformed plane X-Y
Ψ_2	disturbance stream function for transformed plane Z-Y
$\phi_{1(y)}$	disturbance amplitude function for X direction in transformed plane

$\phi_{2(y)}$ disturbance amplitude function for Z direction in transformed plane

α_1 $2\pi/$(wavelength of disturbance in transformed plane in X-direction)

α_2 $2\pi/$(wavelength of disturbance in transformed plane in Z-direction)

μ dynamic viscosity

α proportionality constant for viscosity-temperature relationship

ν kinematic viscosity

Θ momentum thickness in physical s, ξ plane for 2-D or 3-D

normal direction $\Theta = \int_0^\infty \frac{\rho u}{\rho_e u_e} \left(1 - \frac{u}{u_e}\right) d\xi$

$\Theta_{T, X}$ momentum thickness in transformed X, Y plane for 2-D or 3-D

$$= \int_0^\infty \frac{U}{U_e} \left(1 - \frac{U}{U_e}\right) dY$$

$\Theta_{T,Z}$ momentum thickness in transformed Z, Y plane

$$= \int_0^\infty \frac{W}{W_e} \left(1 - \frac{W}{W_e}\right) dY$$

$\Theta_{p,s}$ $\int_0^{\delta_{p,s}} \frac{\rho u}{\rho_e u_e} \left(1 - \frac{u}{u_e}\right) d\xi$

$\Theta_{p,z}$ $\int_0^{\delta_{p,z}} \frac{\rho w}{\rho_e w_e} \left(1 - \frac{w}{w_e}\right) d\xi$

$\Theta_{p,n}$ $\int_0^{\delta_{p,n}} \frac{\rho u}{\rho_e u_e} \left(1 - \frac{w}{w_e}\right) d\xi$

$\delta_{p,n}$ greater of $\delta_{p,s}$ or $\delta_{p,z}$

δ	boundary-layer thickness in physical plane
δ^*	$= \int_0^\delta (1 - \frac{\rho u}{\rho_e u_e}) d\xi$
δ_T	boundary-layer thickness in transformed plane
$\delta_{T,X}^*$	displacement thickness in transformed X, Y plane for 2-D or 3-D
	$\int_0^\infty (1 - \frac{U}{U_e}) dY$
$\delta_{T,Z}^*$	displacement thickness thickness in transformed Z, Y plane
	$= \int_0^\infty (1 - \frac{W}{W_e}) dY$
$\delta_{T,X}^{**}$	$\int_0^{\delta_{T,n}} (1 - \frac{U}{U_e}) \frac{T_e}{T} dY$
$\delta_{T,Z}^{**}$	$\int_0^{\delta_{T,n}} (1 - \frac{W}{W_e}) \frac{T_e}{T} dY$
	$\delta_{T,n}$ greater of $\delta_{T,X}$ or $\delta_{T,Z}$
Λ	local sweep angle in degree
γ	ratio of specific heats for air
η	$= 2y/b$

Subscripts

o	stagnation condition
e,s	edge of boundary layer in s-direction
e,z	edge of boundary layer in z-direction
aw	adiabatic wall condition
m	mean or average value over boundary-layer thickness
N	normal section
p	physical plane

p,s	physical plane in s-direction
p,z	physical plane in z-direction
p,n	either p,s or p,z
s	direction normal to local sweep lines
T	transformed plane
T,X	transformed plane X-direction
T,Z	transformed plane in Z-direction
w	conditions at wall
X	transformed X-direction
Z	transformed Z-direction
L.E.	conditions at leading edge
T.E.	conditions at trailing edge
δ	parameter based on boundary-layer thickness
θ	parameter based on momentum thickness
∞	freestream value
S	measured in streamwise direction

In addition to the above list of symbols and subscripts, symbols and subscripts are also defined at appropriate places in the text.

DESCRIPTION OF THEORY

A description of the theory for the integral methods used to compute the laminar boundary layer, transition, and the turbulent boundary layer on a swept wing is given in references 5, 7, and 8. These theoretical methods were developed for infinite-span swept wings at subsonic and transonic speeds, and for two-dimensional airfoils and bodies of revolution at supersonic speeds. However, they did not include the effects of spanwise pressure gradient and the resulting effects on the location of transition. The boundary-layer "wash-out" phenomena are present on finite aft swept wing configurations with a given taper and twist, whereas the boundary-layer "wash-in" phenomena are present on configurations with forward sweep. The above theoretical methods of references

5, 6, and 7 have been extended in the present paper to account for the effects of spanwise pressure gradients on laminar boundary-layer transition. At the present time, the effects of suction on the extended method are not considered.

The theoretical programs, which have been developed and used in the present theoretical investigations of the wing glove of the F-14 aircraft and for the parametric design studies of the forward swept wing of the X-29 aircraft with a laminar flow glove, are classified and enumerated as follows:

1. Potential/Viscous Design and Analysis

    a. Perturbation Method of Characteristics for inverse design at transonic Mach numbers.

    b. Bauer-Garabedian-Korn Program for transonic analysis.

    c. NASA-Lockheed Multi-component Airfoil Program for subsonic analysis.

2. Boundary-Layer Analysis

    a. Integral Compressible Laminar Boundary-Layer Method with arbitrary chordwise pressure distribution and spanwise pressure gradient, sweep and suction at subsonic through high supersonic speeds.

    b. Short bubble and reattachment criteria.

    c. Instability and transition prediction due to leading-edge-normal and spanwise flow including the effects of spanwise pressure gradient.

    d. Separating turbulent boundary-layer method from subsonic to transonic speeds.

3. Method for computing $C_{D_{wake}}$ for an infinitely swept wing from subsonic through supersonic speeds.

4. Modified strip method to account for the effects of taper, sweep, and twist on wing-section characteristics.

The theoretical development of the laminar boundary-layer method for an infinitely swept wing will be briefly described. In addition, the methodology for determining the effects of spanwise pressure gradients on laminar boundary-layer growth and on transition location will be outlined.

Governing Equations

The usual governing equations for a compressible hydrodynamic boundary layer on an infinitely swept wing for the coordinate axis system shown in figure 1 are the continuity, streamwise momentum in s-direction, and momentum

C - 3

in the ξ and z directions. The coordinate axis of figure 1 is chosen for the purpose of facilitating the application of the present theory to the design of the wing sections for an arbitrary wing planform. Moreover, the determination of the effect of the spanwise pressure gradient on the extent of laminar flow on swept wings by the present methods is greatly facilitated by the use of the coordinate axis system selected. Thus,

$$\frac{\partial(\rho u)}{\partial s} + \frac{\partial(\rho v)}{\partial \xi} = 0 \qquad \text{Continuity} \qquad (1a)$$

$$\rho u \frac{\partial u}{\partial s} + \rho v \frac{\partial u}{\partial \xi} = -\frac{\partial P}{\partial s} + \frac{\partial}{\partial \xi}\left(\mu \frac{\partial u}{\partial \xi}\right) \rightarrow \begin{pmatrix} \text{s-direction} \\ \text{momentum} \end{pmatrix} \qquad (1b)$$

$$\frac{\partial P}{\partial \xi} = 0 \qquad \text{(Normal Momentum)} \qquad (1c)$$

$$\rho u \frac{\partial w}{\partial s} + \rho v \frac{\partial w}{\partial \xi} = +\frac{\partial}{\partial \xi}\left(\mu \frac{\partial w}{\partial \xi}\right) . \qquad \begin{pmatrix} \text{z-direction} \\ \text{spanwise} \\ \text{momentum} \end{pmatrix} \qquad (1d)$$

The above equations (1) contain the terms consisting of variable physical properties, such as density ρ and dynamic viscosity μ. Variations of these properties across the boundary layer as well as along the flow direction are not negligible for laminar boundary-layer flow at transonic speeds and are accounted for. At supersonic speeds, variations in the physical properties are very large which means that there is a strong coupling between solutions of the hydrodynamic and thermal boundary-layer equations.

In order to simplify the governing equations (1) for solution by integral techniques while maintaining realistic computational results for the hydrodynamic and thermal boundary layers, the use of the following Stewartson's transformation is made:

$$X = \int_0^s \alpha \frac{a_e}{a_0} \frac{P_e}{P_0} ds \qquad (2)$$

$$Y = \frac{a_e}{a_0} \frac{\rho_e}{\rho_0} \int_0^\xi \frac{T_e}{T} d\xi$$

where α is the proportionally constant for the viscosity-temperature relationship, namely

$$\frac{\mu}{\mu_0} = \alpha \frac{T}{T_0} \tag{3a}$$

$$\alpha = \left(\frac{T_{aw}}{T_0}\right)^{1/2} \frac{T_0 + 198.6}{T_{aw} + 198.6} \tag{3b}$$

$$\frac{T_{aw}}{T_0} = \frac{(1 + \sqrt{Pr}\ \frac{\gamma-1}{2} M_e^2)}{(1 + \frac{\gamma-1}{2} M_e^2)} \tag{3c}$$

Furthermore, if it is assumed that the viscous flow on the wing can be divided into a finite number of suitably oriented strips on its surface, and that each infinitesimal control volume of the strip is a portion of an infinite-span swept wing, then the governing equations of motion in the physical and transformed planes can be further simplified. The transformed boundary-layer equations using Stewartson's transformations, for infinite-span swept wing conditions, which can be derived from equations (1) with adiabatic wall temperature, are written as,

$$\frac{\partial U}{\partial X} + \frac{\partial V}{\partial Y} = 0 \tag{4a}$$

$$U \frac{\partial U}{\partial X} + V \frac{\partial U}{\partial Y} = U_e \frac{dU_e}{dX} + \nu_0 \frac{\partial^2 U}{\partial Y^2} \tag{4b}$$

$$U \frac{\partial W}{\partial X} + V \frac{\partial W}{\partial Y} = \nu_0 \frac{\partial^2 W}{\partial Y^2}. \tag{4c}$$

The relationships between the velocities within the boundary layer and the pressure gradients in the physical and transformed planes can be written ($Pr \approx 1$) as

$$U = \frac{a_0}{a_e} u; \quad V \simeq \frac{a_0}{a_e} v \quad \text{(for adiabatic wall)}; \quad W = w \tag{5a}$$

$$\frac{dU_e}{dX} = \frac{1}{\alpha} a_0 \frac{dM_e}{ds} \left(1 + \frac{\gamma-1}{2} M_e^2\right)^4 \tag{5b}$$

C-5

while the applicable boundary conditions in the transformed planes are given by,

$$@ \ Y = 0 \rightarrow U = W = 0, \qquad V = V_s = -\frac{a_o}{a_e} v_w \qquad (6a)$$

$$@ \ Y = \delta_{T,X} \rightarrow U = U_e = a_o M_e, \quad \frac{\partial U}{\partial Y} = \frac{\partial^2 U}{\partial Y^2} = 0 \qquad (6b)$$

and

$$@ \ Y = \delta_{T,Z} \rightarrow W = W_e = w_e, \quad \frac{\partial W}{\partial Y} = \frac{\partial^2 W}{\partial Y^2} = 0 \qquad (6c)$$

The compatibility conditions at the surface of the wing in the transformed planes can be written as,

$$@ \ Y = 0 \rightarrow - V_s \left(\frac{\partial U}{\partial Y}\right)_w = U_e \frac{dU_e}{dX} + v_o \left(\frac{\partial^2 U}{\partial Y^2}\right)_w \qquad (7a)$$

$$@ \ Y = 0 \rightarrow - V_s \left(\frac{\partial^2 U}{\partial Y^2}\right)_w = v_o \left(\frac{\partial^3 U}{\partial Y^3}\right)_w \qquad (7b)$$

and in the absence of suction for flows with spanwise pressure gradients,

$$\frac{1}{\rho} \frac{\partial P}{\partial z} \bigg|_{Y=0} = \frac{a_e}{a_o} v_o \frac{\partial^2 W}{\partial Y^2} \bigg|_{Y=0}. \qquad (7c)$$

The integral equations in the transformed planes in the leading-edge normal direction X and in the spanwise direction Z can be derived by making use of equations (4), boundary conditions (6), and wall compatibility conditions equations (7), and by use of Leibnitz's rule.

Momentum Integral Equation in X-Direction, Infinite Swept Wing Conditions

$$U_e \frac{d}{dX} \left(\frac{K}{dU_e/dX}\right) = 2 \left[L - K(H_{T,s} + 2) - S_{\theta_X}\right] \qquad (8)$$

$$\frac{d}{dX}\left[U_e W_e \int_0^{\delta_{T,n}} \frac{U}{U_e}\left(1 - \frac{W}{W_e}\right)dY\right] = \nu_0\left(\frac{\partial W}{\partial Y}\right)_{Y=0} - V_s W_e \qquad (9)$$

where $\delta_{T,n}$ is greater of $\delta_{T,Z}$ or $\delta_{T,X}$.

The symbols L, K, and S_θ appearing in the above equation (8) are defined in equation (20) for transformed X and Z coordinates.

The velocity profile assumptions for the flow in the X- and Z-directions in the transformed planes are given by the following equations,

$$\frac{U}{U_e} = A_1 n_X + A_2 n_X^2 + A_3 n_X^3 + A_4 n_X^4 \qquad (10a)$$

where

$$n_X = \frac{Y}{\delta_{T,X}},$$

and

$$A_1 = 2 + Q_X/6; \qquad A_2 = -0.5Q_X;$$
$$A_3 = -2 - A_2; \qquad A_4 = 3 - A_1 \qquad (10b)$$

$$\frac{W}{W_e} = 2n_Z - 2n_Z^3 + n_Z^4 \qquad (11)$$

where, $n_Z = \frac{Y}{\delta_{T,Z}},$

The numerical solutions of equations (8) and (9) are performed by the Euler method with repeated iterations. These solutions give the shape of velocity profiles $\frac{U}{U_e}$ and $\frac{W}{W_e}$ in the transformed planes under the assumption of infinite-span swept-wing conditions.

EFFECTS OF BOUNDARY-LAYER WASH-IN/WASH-OUT DUE TO SPANWISE PRESSURE GRADIENTS ON TRANSITION ON FINITE, SWEPT, TAPERED, AND TWISTED WING

The results of theory/experiment correlations for several wings using both wind tunnel and flight-test data have indicated that for sweeps greater than approximately 25°, and freestream Reynolds numbers greater than 20 million transition is triggered by spanwise flow in the z direction. Thus, for the purpose of designing laminar-flow wings and gloves at transonic and supersonic speeds at Reynolds numbers and sweeps of practical interest, it is necessary to consider the effects of boundary-layer wash-in/wash-out due to spanwise pressure gradients. This is especially important for wings of supersonic aircraft where the sweep of the leading edge is usually in excess of 45°. In order to account for the effects of boundary-layer wash-in/wash-out on finite swept wings the approach shown schematically in figure 2 is used. This figure shows the infinitesimal control volume composed of surfaces of a trapezoid. The coordinate system is the orthogonal s, ξ and z axes where the s coordinate is normal to the local sweep line, z-coordinate is normal to s in the plane of wing, and the ξ-coordinate is normal to the s-z plane. A_1B_1 and C_1D_1 are constant s/c lines where c is the local chord in s-direction and A_1D_1 and B_1C_1 are parallel to s-direction.

The momentum theorem is applied in the z-direction, which states that the algebraic sum of the forces acting on the control volume $ABCD - A_1B_1C_1D_1$ in the z-direction is equal to the rate of change of momentum in control volume plus the net flux of momentum in the z-direction across the control surfaces of the control volume. For steady mean flow conditions an equation can be derived for the boundary-layer wash-in/wash-out due to spanwise pressure gradient effects on velocity profile $\dfrac{W}{W_e}$ in the z-direction. This equation in the physical coordinate system for transformed boundary-layer quantities can be written as:

$$\frac{1}{2} (\theta_{T,z})_N \frac{dC_p}{dz} = \{ \frac{\partial}{\partial z} [(\theta_{T,z})_0 \frac{W_e^2}{U_\infty^2} (1 + 0.2 M_{e,z}^2)^{0.5}]$$

$$+ \frac{W_e}{U_\infty} \frac{u_e}{U_\infty} (1 + 0.2 M_{e,s}^2)^{0.5} [\frac{1}{M_{e,s}} \frac{d M_{e,s}}{ds} (\delta_{T,X})_0 (0.7 + 0.00833 \Lambda_X)$$

$$+ (0.7 + 0.00833 \Lambda_X) \frac{d}{ds} (\delta_{T,X})_0 + 0.00833(\delta_{T,X})_0 \frac{d\Lambda_X}{ds}]$$

$$- \frac{\mu_w}{\mu_0} \cdot v_0 \cdot \frac{W_e}{U_\infty} \cdot \frac{1}{U_\infty} \frac{1}{(\theta_{T,z})_0} \cdot 0.235 \frac{(1 + 0.2 M_{e,s}^2)^{-3}}{(1 + 0.171 M_{e,s}^2)} \}$$

$$\cdot (1 + 0.2 M_{e,z}^2)^{-3} (1 + 0.2 M_\infty^2)^{2.5} / (8.547 + 0.711 M_{e,z}^2) \qquad (12)$$

where

$(\Theta_{T,Z})_N =$

Transformed momentum thickness in Z-direction which is modified by the boundary-layer wash-in/wash-out phenomena due to spanwise pressure gradients on finite-swept and tapered wing.

$(\theta_{T,Z})_0 =$

Transformed momentum thickness in Z-direction for infinitely swept wing assumption conditions.

$$\Lambda_X = (\delta^2_{T,X})_0 \frac{1}{\nu_0} \frac{dU_e}{dX} =$$

Dimensionless pressure gradient parameter in X-direction in transformed plane for infinite-span, swept-wing assumption conditions.

$(\delta_{T,X})_0 =$

Transformed boundary-layer thickness in X-direction for infinite-span swept-wing assumption condition.

$$\frac{\mu_w}{\mu_0} = \left(\frac{T_{aw}}{T_0}\right)^{1.5} \frac{T_0 + 198.6}{T_{aw} + 198.6}$$

due to Sutherland theory of viscosity.

The following approach is used for the purpose of calculating $(\delta_{T,Z})_N$ and the velocity profiles in the transformed plane in the spanwise direction in order to account for the boundary-layer wash-in or wash-out phenomena.

Define the quantities,

$$\Lambda_{Z_N} = (\delta^2_{T,Z})_N \left(\frac{1}{\nu_0} \frac{dW_e}{dZ}\right)$$

and,

$$\beta_{Z_N} = (\theta^2_{T,Z})_N \left(\frac{1}{\nu_0} \frac{dW_e}{dZ}\right)$$

(13)

where:

$(\delta_{T,Z})_N =$

Transformed boundary-layer thickness in Z direction which is modified by the boundary-layer wash-in/wash-out phenoena due to spanwise pressure gradients on finite-swept and tapered wing.

If a fourth order velocity profile is assumed in the spanwise Z direction in the transformed plane, then the relation between Λ_{Z_N} and β_{Z_N} can be derived as the following polynominal:

180

$$\Lambda_{Z_N} = P_1 + P_2 \beta_{Z_N} + P_3 \beta^2_{Z_N} + P_4 \beta^3_{Z_N} + P_5 \beta^4_{Z_N} + P_6 \beta^5_{Z_N}$$

where,

$$P_1 = 0.032015$$

$$P_2 = 73.156$$

$$P_3 = 10.587$$

$$P_4 = -129.6$$

$$P_5 = 4669.6$$

$$P_6 = 43865.0$$

thus, $(\delta_{T,Z})_N$ can be written as, $(\delta_{T,Z})_N = (\theta_{T,Z})_N / (\beta_{Z_N} / \Lambda_{Z_N})^{1/2}$.

The velocity profile $\dfrac{W}{W_e}$ in the transformed plane can therefore be calculated from the following assumed fourth order polynomial given by:

$$\frac{W}{W_e} = B_1 \eta_Z + B_2 \eta^2_Z + B_3 \eta^3_Z + B_4 \eta^4_Z$$

where,

$$\eta_Z = \frac{Y}{(\delta_{T,Z})_N} \quad \text{and} \quad B_1 = 2 + \frac{\Lambda_{Z_N}}{6}; \quad B_2 = -\frac{1}{2} \Lambda_{Z_N}$$

$$B_3 = -2 - B_2; \quad B_4 = 3 - B_1$$

THERMAL BOUNDARY-LAYER SOLUTION

Temperature variations within the boundary layer at subsonic speeds are small, hence the effects of temperature variations within the boundary layer on instability and transition at subsonic speeds are neglected. However, at high transonic and supersonic speeds, the heat generated by friction and adiabatic compression is quite significant. These phenomena give rise to large temperature variations across the boundary layer, and it has been found from computational experiments that these large temperature variations affect the following equations for computing temperature profiles; they can be derived using the procedures described earlier.

$$\frac{T - T_w}{T_{e_{Y=\delta_{T,X}}}} = \frac{T_w - T_{aw}}{T_{e_{Y=\delta_{T,X}}}} \left(\frac{U}{U_e}\right) - \sqrt{Pr}\, \frac{U_e^2}{2gC_pT_o}\left(\frac{U}{U_e}\right)^2 \tag{14a}$$

$$\frac{T - T_w}{T_{e_{Y=\delta_{T,Z}}}} = \frac{T_w - T_{aw}}{T_{e_{Y=\delta_{T,Z}}}} \left(\frac{W}{W_e}\right) - \sqrt{Pr}\, \frac{W_e^2}{2gC_pT_o}\left(\frac{W}{W_e}\right)^2 \tag{14b}$$

For determining the temperature profile at a given location on the wing use is made of either equations (14a) or (14b) depending upon whether $\delta_{T,X}$ is larger than $\delta_{T,Z}$ or vice versa. The velocity profiles $\frac{U}{U_e}$ or $\frac{W}{W_e}$ in the transformed planes in X or Z direction, which are required in equations (14a) or (14b), are dependent on local pressure gradients in the leading edge normal-s or spanwise-z directions due to use of equations (9) or (11), respectively. Thus, the effect of pressure gradient and suction is implicitly accounted for in the determination of temperature profiles by the present method.

Criteria for Determining Locations of Neutral Instabilities for Velocity Profiles in s and z Directions

The Orr-Sommerfeld equations in transformed planes for X and Z directions can be written as follows: For the transformed coordinate in the X-direction,

$$(U - C_1)(\phi_1'' - \alpha_1^2\phi_1) - U_{YY}\phi_1 = \frac{i}{\alpha_1 R_{\theta_{T,X}}} [\phi_1'''' - 2\alpha_1^2\phi_1'' + \alpha_1^4\phi_1] \tag{15}$$

and for the transformed coordinate in the Z-direction,

$$(W - C_2)(\phi_2'' - \alpha_2^2\phi_2) - W_{YY}\phi_2 = \frac{i}{\alpha_2 R_{\theta_{T,X}}} [\phi_2'''' - 2\alpha_2^2\phi_2'' + \alpha_2^4\phi_2] \tag{16}$$

The disturbance stream functions for the transformed X and Z directions are assumed, as for the physical plane, as the following types:

$$\Psi_1' = \phi_{1(Y)}e^{i\alpha_1(X-C_1t)} \quad \rightarrow \text{X-direction} \tag{17a}$$

$$\Psi_2' = \phi_{2(Y)}e^{i\alpha_2(Z-C_2t)} \quad \rightarrow \text{Z-direction} \tag{17b}$$

182

where,

$\phi_{1(Y)}$ and $\phi_{2(Y)}$ = disturbance amplitude function for X and Z direction, respectively in transformed planes

α_1 and α_2 = $2\pi/$(disturbance wavelength in transformed planes in X- and Z-direction, respectively)

X = transformed coordinate for s-direction

Z = transformed coordinate for z-direction

$$C_1 = C_{1_r} + iC_{1_i}$$

complex in general

$$C_2 = C_{2_r} + iC_{2_i}$$

C_{1_i} or C_{2_i} = 0   corresponds to neutral instability

           > 0   corresponds to amplification of disturbance

           < 0   corresponds to decay of disturbance

The generalized solution between the dimensionless pressure gradient parameters and "equivalent" Reynolds number based on momentum thickness for the neutral stability of laminar boundary layers in either s or z direction is shown in figure 3. The curve shown in this figure is derived from solutions of the Orr-Sommerfeld equations, equations (15) and (16), in the transformed X-Y plane or Z-Y plane for appropriate fourth-order polynomial velocity profiles. The effects of pressure gradient in the s-direction or z-direction, local Mach number, temperature profile, and suction have been accounted for in the derivation of this curve. The abscissa of figure 3 is given as the zero suction (S_θ = 0) version of

$$a_o \frac{1}{\alpha} \frac{1}{\nu} \left\{ \begin{array}{c} \theta_{p,s} \dfrac{dM_{e,s}}{ds} \\ \text{or} \\ \theta_{p,z} \dfrac{dM_{e,z}}{dz} \end{array} \right\} \frac{1}{\left(1 + 0.2 \left\{ \begin{array}{c} M_{e,s}^2 \\ \text{or} \\ M_{e,z}^2 \end{array} \right\} \right)^2} \cdot \left[1 - \frac{S_\theta}{(M + S_\theta \left\{ \begin{array}{c} L_X \\ \text{or} \\ L_Z \end{array} \right\})} \right] \tag{18}$$

where

$$\nu_m = \frac{1}{\delta_n} \int_0^{\delta_n} \nu \, d\xi$$

$$\delta_n = \text{greater of } \delta_{p,s} \text{ or } \delta_{p,z}$$

$$\nu = \nu_0 \left(1 + \frac{\gamma-1}{2} \left\{ \begin{matrix} M_{e,s}^2 \\ \text{or} \\ M_{e,z}^2 \end{matrix} \right\} \right)^{1.5} \cdot \frac{T}{T_{e,s}} \text{ or } T_{e,z} \tag{19}$$

In equation (19), the term $(\frac{T}{T_{e,s}})$ or $(\frac{T}{T_{e,z}})$ for temperature profile are substituted from equations (14a) or (14b).

It should be noted that because of the choice of the coordinate axis systems shown in figures 1 and 2, it is possible to use the same criteria shown in figure 3 for determining the neutral stability point for disturbances in both the normal and spanwise directions.

Boundary-Layer Transition Criteria

The criteria used in the present method for determining the transition location due to the amplification of disturbances either in the normal or spanwise directions are shown in figure 4. The parametric curves of figure 4 are valid for arbitrary specified pressure gradients - both in the normal as well as spanwise directions. The independent and dependent variables shown in this figure contain groups of several hydrodynamic and thermal boundary-layer parameters which are significant during the transition process. In deriving the curve for low values of freestream turbulence (less than .05 percent), the use of experimental data obtained in flight or low-turbulence wind tunnels is made and this information is put in the transformed planes. The dimensionless parameters shown in figure 4 have been derived from dimensional analyses and by making use of the laws of dynamic similarity. These physical dimensionless parameters consist of the following:

$$K_X = \frac{\Theta_{T,X}^2}{\nu_0} \frac{dU_e}{dx} , \quad K_Z = \frac{\Theta_{T,Z}^2}{\nu_0} \frac{dW_e}{dZ}$$

$$L_X = \frac{\Theta_{T,X}}{U_e} \left(\frac{\partial U}{\partial Y}\right)_{Y=0} ; \quad L_Z = \frac{\Theta_{T,Z}}{W_e} \left(\frac{\partial W}{\partial Y}\right)_{Y=0}$$

184

$$M_X = \frac{\theta_{T,X}^2}{U_e} \left(\frac{\partial^2 U}{\partial Y^2}\right)_{Y=0} \quad ; \qquad M_Z = \frac{\theta_{T,Z}^2}{W_e} \left(\frac{\partial^2 W}{\partial Y^2}\right)_{Y=0}$$

$$S_{\theta_X} = \frac{\theta_{T,X} V_s}{\nu_o} \quad ; \qquad S_{\theta_Z} = \frac{\theta_{T,Z} V_s}{\nu_o}$$

$$R_{N_X} = \frac{U_e \delta_n^{**}}{\nu_m} \quad ; \qquad R_{N_Z} = \frac{W_e \delta_n^{**}}{\nu_m}$$

$$\delta_{n_X}^{**} = \int_0^\infty \left(1 - \frac{U}{U_e}\right)\left(\frac{T_e}{T}\right) dn_X ; \qquad \delta_{n_Z}^{**} = \int_0^\infty \left(1 - \frac{W}{W_e}\right)\left(\frac{T_e}{T}\right) dn_Z$$

$$n_X = \frac{Y}{\delta_{T,X}} \quad ; \qquad n_Z = \frac{Y}{\delta_{T,Z}}$$

$$\frac{T}{T_e} = \frac{\text{Temperature}}{\text{Profile}} = F\left(\frac{U}{U_e}, \frac{W}{W_e}, Pr, M_L, \frac{\text{pressure}}{\text{gradient}}\right) \tag{20}$$

In deriving the curves for several higher values of freestream turbulence greater than 0.05% shown in figure 4, use has been made of information presented in figure 5 for a zero pressure gradient and for values of Mach number from low subsonic to high supersonic (up to $M_\infty = 4.0$). It has been hypothesized in constructing the curves of figure 4 for values of freestream turbulence greater than 0.05 percent, that the effect of pressure gradient for freestream turbulence greater than 0.05 is similar to low values of freestream turbulence of 0.05. Curves for freestream turbulence higher than 0.05 percent, shown in figure 4, have been constructed by making use of information in figure 5 and using the above hypothesis.

It needs to be pointed out here that the curves of figure 5 can also be used for other types of disturbances, e.g., noise generated due to the turbulent boundary layer on the walls of the test section of supersonic wind tunnels. This objective can be accomplished after the application of appropriate calibration procedures.

Turbulent Boundary Layer

It has been known from experimental data on sections of NLF wings that if turbulent separation is present upstream of $x/c \approx 0.95$, then the design pressure distribution necessary to maintain laminar flow is degraded. Additionally, the wake drag will be quite high due to presence of the separated flow region. In the present paper turbulent boundary-layer separation is

accounted for by the method developed in reference 8. This turbulent boundary-layer method has already been successfully applied in the design of NLF and HLFC wing sections and for the prediction of wake drag.

To compute the turbulent boundary layer from the location of transition at various spanwise stations to the wing trailing edge, the method of reference 8 was modified to account for effect of spanwise flow assuming infinite swept wing conditions. The important objectives for the computations of the turbulent boundary layer are: (1) to see if turbulent separation is present downstream of the transition location, and (2) to determine the turbulent boundary-layer quantities at the wing trailing edge.

The theoretical method of reference 8 has been developed by analyzing the mean and fluctuating components of velocity profile data obtained by the use of a laser velocimeter for several airfoils with trailing-edge seperation. These experimental data indicated that as the turbulent boundary layer approached the separation location, the fluctuating velocity components become of the same order of magnitude as the mean velocity components within the turbulent boundary layer. This observation suggested the retention of the fluctuating-velocity components in the governing equations of motions as was done in reference 8. This method has been found to be extremely reliable in predicting turbulent boundary-layer quantities, including separation, on wing sections with thickness ratios in the range of $0.09 < t/c < 0.22$ and Reynolds numbers from 2 to 30 million.

Computations of $C_{D_{wake}}$ for Wing Sections

The derivation of the expression for $C_{D_{wake}}$ for an infinitely swept wing is given in Appendix A. This expression, which is valid from subsonic to supersonic speeds, is given as

$$C_{D_{wake}} = \frac{2}{c} \left[(\Theta_{uu})_{T.E.} \left(\frac{\rho_e}{\rho_\infty}\right)_{T.E.} \left(\frac{u_e}{u_\infty}\right)^p \cos^2 \Lambda_{T.E.} \right.$$

$$\left. + (\Theta_{uw})_{T.E.} \left(\frac{\rho_e}{\rho_\infty}\right)_{T.E.} \left(\frac{w_{e_{T.E.}}}{w_\infty}\right) \sin^2 \Lambda_{T.E.} \right]$$

where the exponent p is given by

$$p = [H_{T.E.} + 5 + (\gamma-1)\overline{M_e^2}]/2.0 \qquad (21)$$

The $C_{D_{wake}}$ for a finite tapered swept wing can be computed from equation (21) and by making use of modified strip theory.

186

APPLICATIONS OF THE PRESENT THEORETICAL METHODS

The theoretical methods described in previous sections are utilized to perform two tasks in the following section, namely:

(i) The predition of transition location and turbulent boundary-layer parameters on the "clean-up" glove of the F-14 aircraft and correlation with experimental data.

(ii) Performing parametric studies for the design of a laminar glove for the forward swept wing of X-29 aircraft.

Correlation with Experimental Data on the Glove of F-14 Aircraft

The planform and instrumentation for the gloved F-14 wing with 20° sweep is shown in figure 6. With the "clean-up" glove installed, the sweep of the wing leading edge was varied from $\Lambda_{L.E.} = 20°$ to $\Lambda_{L.E.} = 35°$, and the flaps and slats were locked in the up position. As shown in figure 6, the three rows of surface pressure orifices are located at spanwise stations $\eta = 0.515$, 0.67, and 0.83, respectively, and were oriented in a direction parallel to freestream for the wing leading edge sweep $\Lambda_{L.E.} = 20°$. In order to avoid interference between hot-film gauges, they were placed at an angle of 30° to rows of surface pressure orifices as shown in this figure. The boundary-layer rakes were installed at two spanwise locations at $x/c = 0.55$ in order to measure the turbulent boundary-layer velocity profiles. Transition and turbulent boundary-layer data were obtained for freestream Mach numbers from 0.6 to 0.8, wing leading edge sweeps from 20° to 35°, and a Reynolds number range of 8×10^6 to 25×10^6. Pressure distributions for the aforementioned three spanwise locations were also measured for these Mach numbers and sweeps. These pressure distributions constituted the boundary conditions for computing both the laminar and turbulent boundary layers and the transition location on the F-14 glove.

Figure 7(a) shows the pressure distributions on the upper surface of the glove at three spanwise locations and hot film traces at station 2 ($\eta = 0.67$) for the wing leading edge sweep of 20°, $M_\infty = 0.7$ and a freestream Reynolds number based on chord of 13 million. In addition to using the pressure distributions as boundary conditions, they are used to evaluate the effect of spanwise pressure gradient on the development of the laminar boundary layer and transition location at station 2. Since the experimental pressure data only extended back to $x/c = 0.6$ theoretically computed pressures distributions were used from $x/c = 0.6$ to trailing edge in order to compute the growth of turbulent boundary layers from the transition location to the trailing edge. Figure 7(b) shows the computed results for chordwise transition and instability location due to normal flow (N.F.) and spanwise flow (S.F.) phenomena. The results are plotted in this figure as x/c of instability and transition versus freestream Reynolds number. These results indicate that at a Reynolds number of 13 million, the computed transition

location is due to N.F. phenomena and occurs at $x/c = 0.33$. The hot film trace shown in figure 7(a) shows that the experimental transition location at station 2 is between $0.3 < x/c < 0.4$. Thus, good agreement is obtained between the theoretically computed transition location and the hot-film-measured transition location. Figure 7(c) shows the results of computations for displacement thickness, δ^*/c, momentum thickness, θ/c, and form factor H, plotted against x/c for station 2. Freestream Mach number, Reynolds number, and leading edge sweep for the results shown in figure 7(c) are the same as for figures 7(a) and 7(b). Experimental data for δ^*/c, θ/c, and H at $x/c = 0.55$ for station 2 in the turbulent boundary-layer region are also plotted in figure 7(c). These results indicate that present theoretical computations for the turbulent boundary-layer parameters agree quite well with the experimentally measured quantities. Furthermore, these results indicate that the location of transition predicted by the present theory must be in close agreement with experimentally determined transition. It is also interesting to notice from figure 7(c) that the slope of θ/c versus x/c in the laminar flow region is smaller than that in the turbulent region. This large slope of θ/c versus x/c in the turbulent boundary-layer region will lead, of course, to large values of θ/c at the wing trailing edge. The wake drag coefficient, $C_{D_{wake}}$, is directly proportional to the momentum thickness, θ/c, at the trailing edge.

Figures 8(a) and 8(b) show plots of experimental pressure distributions and hot film traces for $M_\infty = 0.801$, a leading edge sweep of 20^0 and freestream Reynolds numbers of 11 million and 23 million, respectively. As can be seen from the comparison of pressure distributions in figures 8(a) and 8(b), there is not any noticeable difference in pressure distributions between Reynolds numbers of 11 and 23 million, and hence, the same pressure distributions at three spanwise stations were used for computations of transition and instability results for the range of Reynolds number shown in figure 8(c). These pressure distributions indicate that the shock strength is high, and for this reason, there seems to be some discrepancy in computed and measured turbulent boundary-layer parameters at $x/c = 0.55$, as shown in figure 8(e), even though the transition location is predicted quite accurately. The present shock boundary-layer model is being refined in order to provide better initial conditions for turbulent boundary-layer computations downstream of a strong shock.

As seen from figure 8(c), the computed transition location for a freestream Reynolds number of 11 million is at $x/c \approx 0.5$ and caused by N.F. phenomena, however, at a freestream Reynolds number of 23 million the computed results indicate that transition is caused by S.F. phenomena and occurs at $x/c = 0.41$. Experimental data from the hot film sensor shown in figure 8(a) indicate that at a Reynolds number of 11 million, transition occurs at $x/c \approx 0.5$. Hot film traces at a Reynolds number of 23 million, which are shown in figure 8(b), indicate that transition is occurring, for this freestream condition, at $x/c \approx 0.4$. Thus, as seen from comparisons of

computed results, shown in figure 8(c), with hot film traces of figures 8(a) and 8(b), the present theory reliably predicts both the location of transition as well as its mode, i.e., due to N.F. or S.F. phenomena. Figure 8(d) shows a plot of computed $C_{D_{wake}}$ as a function of freestream Reynolds number. As seen from this figure, $C_{D_{wake}}$ decreases as the freestream Reynolds number increases from 8 to 20 million and above the Reynolds number of 20 million $C_{D_{wake}}$ increase with Reynolds number. The Reynolds number of 20 million, where the computed $C_{D_{wake}}$ becomes minimum, corresponds to the initial triggering of transition due to spanwise flow. This is an important phenomena and one that can be used to advantage as seen in the design of a proposed laminar glove for X-29 aircraft discussed subsequently in this paper. Finally, figure 8(e) shows the plots of computed values of δ^*/c, θ/c and H versus x/c for a Reynolds number of 12.4×10^6.

Figure 9(a) shows the experimental pressure distributions and hot film traces for a wing-glove leading-edge sweep of 25^0, a freestream Mach number of 0.706 and a Reynolds number of 11 million. By using the experimental pressure distributions as boundary conditions (see figure 9(a)), the transition and instability locations are computed and the results are shown plotted in figure 9(b) as a function of freestream Reynolds number. Experimental data for transition obtained from hot film traces, shown in figure 9(a), indicate that transition for a wing glove leading edge sweep of 25.3^0, Reynolds number of 11 million, and $M_\infty = 0.706$ takes place for 0.4 < x/c < 0.5. Theoretical results for these same conditions shown in figure 9(b) also show that transition should occur at an x/c between 0.4 to 0.5.

Now, it is generally believed that if the freestream Mach number is kept constant, that increasing wing sweep reduces the extent of laminar flow. However, experimental data and calculations for the wing-glove leading-edge sweep of 20^0 and $M_\infty = 0.7$, (figures 7(a) and 7(b)) when compared to results for a sweep of 25°, figures 9(a) and 9(b), show that transition is located closer to the leading edge for the lower sweep. Furthermore, comparison of the calculated results of figure 9(b) with those of figure 7(b) indicates the same phenomena. This is an unusual result and shows the ability of the present methods to optimize wing section geometries and planforms for extensive laminar flow regions at specified freestream conditions.

Figure 9(c) shows the results of theoretical computations for the laminar and turbulent boundary-layer parameters δ^*/c, θ/c and H plotted versus x/c for a leading-edge sweep of 25^0, M_∞ of 0.704 and a Reynolds number of approximately 11 million. For this case, strong shocks are not present at any spanwise station, as can be seen from figure 9(a). The computed boundary-layer parameters agree quite well in the turbulent boundary-layer region at x/c = 0.55. This agreement of computations with experiment in the turbulent boundary-layer region is an indication that the computed transition location

189

is fairly close to the experimental transition location. Moreover, these results indicate the reliability of the present theoretical turbulent boundary-layer method.

Figure 10(a) shows the experimental pressure distributions and hot film traces for a leading-edge sweep of 29.7°, $M_\infty = 0.704$, and a Reynolds number of 9.5 million. The corresponding experimental data for a Reynolds number of 19.2 million and leading edge sweep of 31.4° are shown in figure 10(b). Figure 10(c) shows theoretical results for instability and transition locations for a leading-edge sweep of 30° and $M_\infty = 0.704$. These results show that for a Reynolds number of 9 million transition takes place at x/c = 0.34 and is caused by S.F. instability phenomena. Experimental data obtained by hot-film sensors, shown in figure 10(a), for a Reynolds number of 9 million indicate similar results, namely transition takes place at an x/c between 0.3 to 0.4. At a Reynolds number of 19.2 million (figure 10(c)), transition due to S.F. takes place at x/c $\approx$ 0.175; experimental hot film trace data for the same freestream conditions, shown in figure 10(b), also indicate that transition occurs between x/c of 0.1 to 0.2.

Design and Parametric Studies for Laminar Glove of X-29 Aircraft

It has been observed from theoretical studies and experimental data that wing sweep have a pronounced effect on transition location when the freestream Mach number and Reynolds number are held constant. It is also believed by many, from a conceptual view point, that it is easier to achieve large laminar-boundary-layer-flow regions on a forward swept wing (FSW) than on an aft swept wing (ASW). This is so because for FSW the local values of sweep are lower near the leading edge and the local sweep angle increases from the leading edge to the trailing edge; whereas, for ASW, sweep angle is the largest near the leading edge and decreases progressively toward the trailing edge. Figure 11(a) shows schematically a comparison of planforms for "equivalent" FSW and ASW. The word "equivalent" implies that for both FSW and ASW, wing area, aspect ratio, taper ratio, and shock locations are identical. Figure 11(b) shows the plots of local sweep angle versus x/c for FSW and ASW of aspect ratio of 4 and taper ratio of 0.4. The planform and variation of sweep angle with x/c shown in figures 11(a) and 11(b) are a rough approximation of the X-29 aircraft wing. The point C in figure 11(b), which is at the intersection of local sweep versus x/c curves for the "equivalent" FSW and ASW, indicates that the local sweep angles for these "equivalent" wings become equal at x/c $\approx$ 0.5. Thus the possibilities of maintaining laminar flow for x/c < 0.5 on an NLF glove for the FSW of X-29 aircraft are much greater than they would be for an "equivalent" ASW with a laminar glove.

It is possible to realize an additional advantage from forward swept wings and this stems from the lower shock-wave drag. If the NLF design pressure distribution is such that the minimum C_p on the upper surface occurs aft of x/c $\approx$ 0.5, then the local Mach number at the shock location for FSW

will be lower than that ahead of the shock on an "equivalent" ASW for the same value of the freestream Mach number. This is so because the local sweep angle for FSW is higher than that for an equivalent ASW downstream of point C $(x/c \approx 0.5)$ as can be seen from figure 11(b). These phenomena would result in lower shock wave drag for FSW for the NLF design glove of X-29 aircraft, and moreover, the susceptibility of the NLF design for FSW to turbulent separation is also diminished. This is because the initial turbulent boundary-layer thickness at the shock location would be lower for the FSW than for the equivalent ASW.

The above discussion suggests that better prospects exist for overall lower total drag for an NLF concept with FSW than one with an equivalent ASW. The superior drag peformance due to application of NLF (or HLFC) concepts to a FSW arise due to the possibility of achieving larger chordwise runs of laminar boundary-layer flow, lower shock wave drag, and less susceptibility to turbulent separation drag.

Figure 12 shows the planform of the X-29 aircraft. The canard and wing are in the same plane. The wing has a leading-edge sweep of approximately 29° and the trailing-edge sweep is 45°. The chord of the first flap extends from $x/c = 0.75$ to $x/c = 0.9$ and that of the second flap extends from $x/c = 0.9$ to $x/c = 1.0$. The wing leading-edge break is at $\eta = 0.25$, and the tip of the canard is at $\eta = 0.49$. Experimental pressure distributions on the canard suggest that boundary-layer flow separation exists on the canard and the possibility exist that the separated wake of the canard may prohibit the achievement of laminar flow on the wing between the wing root and the midspan location. The forward swept wing has associated with it the boundary-layer wash-in phenomenon, and for this reason it is believed that a laminar glove can be designed so as to obtain extensive laminar flow on the outboard wing from $\eta = 0.55$ to $\eta = 0.95$.

Simple-sweep methods or modified simple-sweep methods are frequently used in the design of airfoil sections for aft swept wings. Different forms of modified simple-sweep methods are employed but they give essentially the same results. The present modified simple sweep approach for ASW is illustrated in figure 13. The geometry of the normal section is arrived at from the geometry of the streamwise section by the following expression:

$$(z/c)_{\text{Normal section}} = \frac{(z/c)_{\text{streamwise section}}}{\cos \Lambda_L}$$

where,

$$\Lambda_L = \text{local value of sweep}$$

$$= \Lambda_{LE} + (\Lambda_{TE} - \Lambda_{LE}) \cdot (x/c)$$

The pressure distribution is computed for the normal section by airfoil programs, such as, Bauer, Garabedian, and Korn program (ref. 9) or Lockheed-NASA multi-Component airfoil program (ref. 10). The computations for the normal section Mach number and lift coefficient are made using

$$M_{\infty_N} = M_{\infty_S} \cdot Cos\Lambda_{effective}$$

where,

M_{∞_N} = effective component of freesteram Mach number for normal section

M_{∞_S} = streamwise freestream Mach number

and, $\Lambda_{effective}$ = Λ @ x/c = 0.25 for subsonic and transonic freestream

Mach numbers

and

$$C_{L_N} = C_{L_S} /Cos^2\Lambda_{effective}$$

where,

C_{L_N} = lift coefficient for normal section

C_{L_S} = lift coefficient for streamwise section

The thickness of the normal section for the aft wing section is thus greater than that of the streamwise section by the factor of $1/Cos\Lambda_L$. The pressure distribution computed for this normal section (with $M_{\infty_N} = M_{\infty_S} Cos\Lambda_{eff}$ and $C_{L_N} = C_{L_S} / Cos^2\Lambda_{eff}$) is related to the pressure distribution for the streamwise section by,

$$C_{P_{Streamwise}} = C_{P_{Normal}} \cdot Cos^2\Lambda_L$$

The application of the above-mentioned modified sweep approach to the computation of the pressure distribution for the forward swept wing of the X-29 at $\eta = 0.7$, $M_\infty = 0.91$ and $C_N = 0.351$ is shown in figure 14. It is apparent from this figure that the theoretical pressure distribution computed by the above-mentioned modified simple sweep method for aft swept wings does not agree with the experimental data for the FSW of X-29 aircraft. Consequently a new modified simple sweep approach was developed for the computation of pressure distributions for forward swept wings. In this approach, the ordinates of the upper surface of the normal section are kept

the same as for the streamwise section but the thickness distribution for the normal section is increased by the cosine of the local sweep angle and is given by

$$(t/c) \text{ Local Normal Streamwise} = (t/c) \text{ Local Streamwise Section} / \cos\Lambda_L$$

The remaining steps for the computation of the streamwise pressure distribution are the same as for the aft swept wing. Both procedures are illustrated in figure 13. The results of computations of the streamwise pressure distributions, using the new modified simple sweep method, for the X-29 aircraft for $\eta = 0.7$, $M_\infty = 0.91$ and $C_L = 0.351$ are shown in figure 14. As seen in this figure, the agreement between the theoretical upper surface pressure distribution computed by the new modified simple sweep method and experimental data is reasonably good. Hence, the parametric studies for the design of the outboard laminar-glove sections are conducted using this approach.

In order to enlarge the extent of laminar flow for the X-29 wing, by the installation of a wing glove, it is first necessary to determine the extent of laminar flow on the existing X-29 wing. Theoretical computations for instability and transition locations on the existing X-29 wing at $\eta = 0.7$ are plotted in figure 15(a) as a function of freestream Reynolds number. Experimental pressure distributions are used for boundary conditions in this calculation. The computed wake drag coefficient for the existing wing section at $\eta = 0.7$ is plotted as a function of freestream Reynolds number in figure 15(b). The results shown in figures 15(a) and 15(b) illustrate that the extent of laminar flow on the existing X-29 wing is quite limited and, consequently, the wake drag is high for Reynolds numbers in the range of 8 to 30 million.

A number of pressure distributions and corresponding glove geometries have been theoretically investigated in the present studies, under the assumption of infinite-span swept-wing conditions. It is necessary that the glove geometry be compatible with original X-29 wing such that the glove wraps the wing surface with continuous first and second derivatives, and that there be a smooth merging of the glove with the original wing surface. From these considerations, the glove with the geometrical shape designated as XTM2P3K, and shown in figure 16 for spanwise station $\eta = 0.7$ was developed. The geometry of the baseline X-29 for the spanwise station of $\eta = 0.7$ is also shown in figure 16 for comparison purposes. Figure 17(a) shows the computed streamwise pressure distribution for this glove at $\eta = 0.7$ for $M_\infty = 0.905$, $C_{L_S} = 0.435$ and a leading-edge sweep of 30^0. The computed pressure distribution for $C_{L_S} = 0.351$ for the baseline section is also shown in figure 17(a) for comparison. It is important to note the shape of $C_{p_{sonic}}$ in figure

193

17(a). For the forward swept tapered wing, the $C_{p_{sonic}}$ line has an upward slope, whereas for the "equivalent" ASW the $C_{p_{sonic}}$ line will have a downward slope. These phenomena suggest, for the specified freestream Mach number and value of C_p just upstream of the shock, that the FSW will have a smaller value of shock wave drag than the ASW.

The streamwise pressure distribution computed for the glove with a L.E. sweep of 25^0, and C_{L_S} = 0.43 is shown in figure 17(b); since the sweep is lower, the design freestream Mach number was lowered to a value of 0.865 (as compared to an M_∞ of 0.905 for sweep of 30^0). The reason that the Mach number was lowered was to keep the leading-edge normal Mach numbers constant. The theoretical transition characteristics for the X-29 glove for leading-edge sweeps of 30^0 and 25^0 and zero spanwise pressure gradients are shown in figure 17(c). As seen from figure 17(c), the S.F. instability triggers the transition at a Reynolds number of 12 million for a leading edge sweep of 30^0, and at a Reynolds number of 15 million for a leading edge sweep of 25^0.

Figure 17(d) shows a comparison of the wake drag characteristics for the X-29 glove for leading edge sweeps of 30^0 and 25^0. Also plotted in figure 17(d) is the wake drag of the baseline section for a leading-edge sweep of 30^0. These comparisons indicate the following phenomena, first, the wake drag of the glove is lower than the basic X-29 wing section by as much as 17 to 18 counts at a Reynolds number of 10.5 million, and second, when the leading-edge sweep is reduced from 30^0 to 25^0, the freestream Reynolds number at which $C_{D_{wake}}$ becomes minimum is increased from 10.5 million to 16 million. However, it may not be possible to reduce the wing glove leading-edge sweep to 25^0 because of stability and control considerations.

As stated previously in the theoretical section, the methods of references 5, 6, and 7 have been extended in the present studies to take into account the effects of boundary-layer wash-in/wash-out and spanwise pressure gradients on the development of the laminar boundary layer as well as instability and transition locations. Thus, it was possible to conduct parametric studies on the effects of boundary-layer wash-in phenomena and spanwise pressure gradients on the triggering of transition due to S.F. phenomena. Proper use of spanwise gradients can delay transition to higher Reynolds numbers and result in a wake drag reduction at the cruise Reynolds number. Figures 18(a) and 18(b) show the two types of spanwise pressure gradients which have been utilized to study the effect of spanwise pressure gradients on transition. In figure 18(a), constant spanwise pressure gradients are assumed on the upper surface from 0 < x/c < 0.6; computations have been performed for spanwise gradients, ΔC_{p_c}, of 0.05, 0.1 and 0.15. For the linearly varying spanwise pressure gradients depicted in figure 18(b), the spanwise pressure gradient is a maximum near the leading edge and it decreases

194

linearly to zero at x/c = 0.6. Computational results are presented for ΔC_{p_1} values of 0.05, 0.1, and 0.15. Instabilities and transition characteristics due to N.F. and S.F. and wake drag characteristics for the various spanwise pressure gradients shown in figures 18(a) and 18(b) have been determined. A few representative results are shown in figures 19 and 20. Figure 19 shows the plots of N.F. and S.F. transition characteristics for a constant spanwise pressure gradient corresponding to ΔC_{p_c} = 0.15. Also plotted in figure 19 for comparison are the results for N.F. and S.F. transition characteristics on the laminar-flow glove for a spanwise pressure gradient of zero. It can be seen from these results that the Reynolds number at which S.F. triggers transition increases from 12 to 20 million as the spanwise pressure gradient is changed from zero to ΔC_{p_c} = 0.15 (see figure 18(a)). Furthermore, notice the change in N.F. transition characteristics for these two cases. Calculations indicate that turbulent separation does not occur in either of the cases shown in figure 19.

Figure 20 shows the plots of $C_{D_{wake}}$ versus freestream Reynolds number for the various constant spanwise gradients, including zero, considered in the present study. Thus, the results shown in figure 20 illustrate the ability of the present theory for increasing the design Reynolds number for minimum wake drag by controlling spanwise pressure gradients. It is necessary to point out here that constant spanwise pressure gradient increases the shock strength of the inboard spanwise location, η = 0.49 and decreases it at the outboard station, η = 0.91. It is likely that these shock strengths (figure 18(a)) will yield different pressure recoveries than that assumed.

Another way to obtain a spanwise gradient is to fix the shock strength and vary the pressure levels near the leading edge. Figure 21 shows the computational results for transition due to N.F. and S.F. phenomena for such a pressure distribution i.e., the linearly varying spanwise pressure gradient, shown in figure 18(b) (ΔC_{p_1} = 0.15) . Also shown in figure 21 are the theoretical transition characteristics for an X-29 glove when the spanwise pressure gradient is assumed to be zero (infinite-span swept wing conditions). Results of figure 21 illustrate that the triggering of transition due to S.F. is delayed from a Reynolds number of 12 million to 16 million due to the effect of spanwise pressure gradient. In addition, the shock strength remains constant along the span when the linearly varying spanwise pressure gradient is assumed. Thus, when the linearly varying spanwise pressure gradient is specified, the shock wave drag remains the same as for a zero spanwise pressure gradient, and also the adverse effect of increased shock strength on the laminar glove design is eliminated.

Figure 22 shows the plots of computed $C_{D_{wake}}$ versus freestream Reynolds number for linearly varying spanwise pressure gradients for several values of ΔC_{P_1}. Also shown are computations for a spanwise pressure gradient of zero for comparison purposes. The results shown in figure 22 further illustrate how the present theory can be used for delaying transition Reynolds number due to triggering of S.F. instabilities by approximately 6 million above the zero spanwise-pressure gradient value by the use linearly varying spanwise pressure gradients. Neither induced drag, C_{D_i}, or shock wave drag are adversely affected.

Comparison Between Equivalent Forward and Aft Swept Wing Concepts for Laminar Flow

A comparison of planforms and local sweep variations for FSW and ASW with an aspect ratio of 4 and a taper ratio of 0.4 is shown in figure 11. The pressure distribution and spanwise pressure gradient selected for making a comparison of laminar flow regions on equivalent FSW and ASW is a linearly varying spanwise pressure gradients with $\Delta C_{P_1} = 0.15$. This spanwise pressure gradient corresponds approximately to that provied by an elliptical spanwise load distribution for both FSW and equivalent ASW. The results of computations for transition locations as a function of the freestream Reynolds number for these "equivalent" wings are shown in figure 23(a) and calculations of $C_{D_{wake}}$ versus freestream Reynolds number are shown in figure 23(b). Figure 23(a) shows that extent of laminar flow for FSW is 15 to 35 percent more than the equivalent ASW for Reynolds numbers from 8 to 30 million. The wake drag for FSW at freestream Reynolds number of 16 million, which corresponds to flight condition for the X-29 aircraft at $M_\infty = 0.905$ and $C_L = 0.435$, is lower by 21 counts than the equivalent ASW.

The comparison shown in figures 23(c) and 23(d) assumes a favorable spanwise pressure gradient that provides a spanwise flow that is opposite to that normally obtained on ASW; this provides a spanload that deviates from the elliptical and causes an increase in C_{D_i} for ASW. Results of computations of the extent of laminar flow, shown in figure 23(c), indicate the extent of laminar flow for FSW is still larger by 7 to 20 percent over the "equivalent" ASW. A comparison of $C_{D_{wake}}$ values under this assumption, as shown in figure 23(d), indicates that for ASW the minimum value of $C_{D_{wake}}$ occurs at a Reynolds number of 11.5 million, whereas for FSW, $C_{D_{wake}}$ becomes a minimum at a freestream Reynolds number of 16.5 million. Moreover, values of $C_{D_{wake}}$ for the range of Reynolds number from 8 to 30 million are lower for FSW than the equivalent ASW.

196

It is necessary to point out that even though the FSW concept, in general, is better for a laminar-flow wing than the equivalent ASW, it is possible to determine other pressure distributions and spanwise pressure gradients for ASW that yield larger extents of laminar flow than shown in figure 23. The insight for obtaining the conditions for large laminar flow regions for highly swept ASW, especially for supersonic flow conditions, can be obtained by going through an optimizaiton process for chordwise pressure distribution and spanwise pressure gradients as has been done for FSW of X-29 aircraft in the present studies.

CONCLUDING REMARKS

(1) The present integral methods for computing laminar boundary-layer properties and transition have been extended to take into account boundary-layer wash-in/wash-out phenomena and the effects of spanwise pressure gradient on transition for the purpose of delaying transition due to S.F. instabilities.

(2) The above method has been applied to predict transition phenomena on the clean-up glove of the F-14 aircraft. Good agreement has been obtained between the predicted location of transition and experimental data as a function of Reynolds number, Mach number, and wing leading edge sweep. The results of the present studies for the F-14 aircraft wing glove, as well as those of references 5, 6, and 7, indicate that once transition occurs due to S.F., the transition location moves upstream very fast with even slight increase in freestream Reynolds number. Thus, by the use of the present method the wing-section geometry can be designed and spanwise pressure gradient specified in such a manner that transition due to S.F. pheonomena can be substantially delayed. This facilitates obtaining larger laminar-flow regions and making the wing performance less susceptible to minor changes in Reynolds number and Mach number.

(3) Comparisons of the computed displacement thicknesses, momentum thicknesses, and form factors in turbulent boundary-layer regions on the glove of a F-14 aircraft by the present turbulent boundary-layer method with experimental data for several freestream conditions and wing sweeps indicated good agreement. This implies that not only is the present turbulent boundary-layer theory quite reliable, but the transition location prediction is accurate as well.

(4) The extent of laminar flow computed for the F-14 wing glove for a leading-edge sweep of 25° and $M_\infty = 0.7$ was larger than that computed for the smaller sweep value of 20°. The experimental data obtained from hot film traces also revealed this unusual pheonomena. This provides additional evidence of the ability of the present method to optimize wing sections as well as the planforms for obtaining large extents of laminar flow.

(5) The effective sweep procedure which is normally used for ASW, when used to compute the streamwise pressure distribution on the FSW of the X-29 aircraft, did not yield good correlation with experimental results. The new effective sweep procedure established during the present study for FSW gives reasonable predictions of streamwise pressure distributions when compared to experimental data for the X-29 wing.

(6) By the use of the method of characteristics, in conjunction with the effective sweep procedure established for FSW, section geometries were established for the outboard glove for the wing of the X-29 so as to obtain the desired chordwise pressure distributions for leading-edge sweeps of 30^0 and 25^0. The computed transition and wake drag characteristics were also computed and compared for these sweeps. The methods were also used to compute transition and wake drag for the basic outboard wing section. This was done for assumed "infinite-span swept-wing" conditions. The wake drag for the investigated glove section was quite superior to the basic section, and the glove with a leading-edge sweep of 25^0 had a minimum value of $C_{D_{wake}}$ at freestream Reynolds number of 16 million as compared to 10.5 million for a sweep of 30^0.

(7) Several spanwise pressure gradients, both constant and linearly varying, for $x/c = 0$ to $x/c = 0.6$ on the upper surface gloves, were investigated for their ability to delay the transition due to S.F. phenomena at $M_\infty = 0.905$.   It was concluded from these parametric studies that both linearly varying and constant-increment spanwise pressure gradients provided beneficial effects on skin friction drag at the flight condition considered.

(8) Computational experiments were performed to determine the extent of laminar flow on FSW and "equivalent" ASW for identical chordwise pressure distributions and spanwise pressure gradients. This comparison indicated that the FSW concept is superior for achieving large regions of laminar flow and lower wake drag than an "equivalent" ASW concept.

APPENDIX A

Expression for Wake Drag for Infinitely Swept Wing
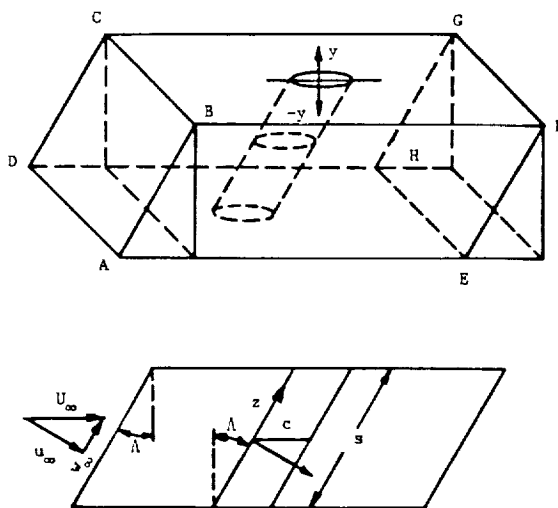
Figure A1. - Coordinate system used for wake drag derivations.

Consider control volume ABCD-EFGH as shown in figure A1 above for a wing with sweep angle Λ. The x-coordinate is perpendicular to the leading edge, the z-coordinate is parallel to leading edge, the y-coordinate is perpendicular to the wing surface, S is equal to wing span as shown, and c is the chord of wing in the direction of flow.

Net mass balance
across the control = $\int_{-\infty}^{\infty} \rho_\infty U_\infty S \cos \Lambda \, dy - \int_{-\infty}^{\infty} \rho u S \, dy = 0$ (A1)
volume

Drag = Net momentum flux across control volume

$$= \int_{-\infty}^{\infty} \rho U_\infty^2 \, S \cos \Lambda \, dy - \int_{-\infty}^{\infty} \rho u S (u \cos \Lambda + w \sin \Lambda) dy \qquad (A2)$$

Multiply equation (A1) by U_∞ and subtract from (A2)

$$\text{Drag} = \int_{-\infty}^{\infty} \rho U_\infty \, uS(\cos^2 \Lambda + \sin^2 \Lambda)dy - \int_{-\infty}^{\infty} \rho uS(u \cos \Lambda + w \sin \Lambda)dy$$

$$= S \cos \Lambda \, \rho_\infty u_\infty^2 \int_{-\infty}^{\infty} \frac{\rho u}{\rho_\infty u_\infty} \left(1 - \frac{u}{u_\infty}\right)dy$$

$$+ S \sin \Lambda \, \rho_\infty u_\infty w_\infty \int_{-\infty}^{\infty} \frac{\rho u}{\rho_\infty u_\infty} \left(1 - \frac{w}{w_\infty}\right)dy \tag{A3}$$

or

$$C_{D_{wake}} = \frac{\text{Drag}}{\frac{1}{2} \rho_\infty U_\infty^2 \, S \cdot c \, \cos \Lambda}$$

$$= \frac{\text{Drag}}{\frac{1}{2} \rho_\infty u_\infty^2 \, \sec^2 \Lambda \cdot S \cdot c \, \cos \Lambda}$$

$$= 2\left\{ \frac{\theta_{uu_\infty}}{c} \cos^2 \Lambda + \frac{\theta_{uw_\infty}}{c} \sin^2 \Lambda \right\} \tag{A4}$$

where

$$\theta_{uu_\infty} = \int_{-\infty}^{\infty} \frac{\rho u}{\rho_\infty u_\infty} \left(1 - \frac{u}{u_\infty}\right)dy$$

$$\theta_{uw_\infty} = \int_{-\infty}^{\infty} \frac{\rho u}{\rho_\infty u_\infty} \left(1 - \frac{w}{w_\infty}\right)dy$$

For swept wings as well as bodies of revolution the boundary-layer parameters at the trailing edge can be calculated by the theoretical methods described in the main body of this paper. Equation (A4) gives $C_{D_{wake}}$ in terms of conditions downstream at infinity. The following derivations show

how boundary-layer parameters at the trailing edge are related to viscous flow quantities at infinity.

The momentum integral equation in the wake in the streamwise direction, either for swept wing or for body of revolution can be written as

$$\frac{d\theta_x}{dx} + \frac{\theta_x}{u_e} \frac{du_e}{dx} \left(2 + \frac{\delta^*_x}{\theta_x}\right) + \frac{1}{\rho_e} \frac{d\rho_e}{dx} \theta_x = 0 \tag{A5}$$

where

$$\theta_x = \theta_{uu} \text{ of equation (A4)}$$

200

By integrating equation (A5) in the wake from the trailing edge to downstream infinity, and after algebraic manipulations the following equation is obtained

$$\left[\ell n \left\{ \theta_x \, \rho_e \left(\frac{u_e}{u_\infty}\right)^{(H_x+2)} \right\} \right]_{T.E.}^{\infty} = \int_{T.E.}^{\infty} \ell n\left(\frac{u_e}{u_\infty}\right) dH \tag{A6}$$

The hypothesis is made that in the wake the following relationship is valid.

$$\ell n \, \frac{U_{e_T}}{U_{\infty_T}} = \ell n \, \frac{U_{e_T}}{U_{\infty_T}}\Bigg|_{T.E.} \cdot \frac{H_{x_T} - 1}{H_{x_T}\Big|_{T.E.} - 1} \tag{A7}$$

The following equation can be derived by making use of Stewartson's transformation for a Prandtl number equal to one.

$$H_x = H_{T_x} \left(1 + \frac{\gamma-1}{2} M_e^2\right) + \frac{\gamma-1}{2} M_e^2 \tag{A8}$$

H_x = streamwise form factor in physical plane

H_{x_T} = streamwise form factor in transformed plane

Substitution of equations (A7) and (A8) into (A5) and simplification results in the following equation

$$\theta_{uu_{(\infty)}} = \theta_{uu_{T.E.}} \cdot \frac{\left(1 + \frac{\gamma-1}{2} M_{e,s}^2\right)_{T.E.}^{-2.5}}{\left(1 + \frac{\gamma-1}{2} M_\infty^2\right)^{-2.5}} \cdot \left(\frac{u_{e_{T.E.}}}{u_\infty}\right)^p \tag{A9}$$

where,

$$p = \{H_{T.E.} + 5 + (\gamma-1)\overline{M_e^2}\}/2$$

$\sqrt{\overline{M_e^2}}$ Root mean square Mach number in the wake from trailing edge to infinity downstream

Equation (A4) for $C_{D_{wake}}$ for a swept wing contains the crossflow momentum thickness term, θ_{uw_∞}. In order to evaluate this crossflow component of momentum thickness, use is made of the momentum equation in the spanwise direction for an infinite-span swept wing. Thus,

$$\rho u \frac{\partial w}{\partial x} + \rho v \frac{\partial w}{\partial y} + \rho w \frac{\partial w}{\partial z} = -\frac{\partial p}{\partial z} + \frac{\partial}{\partial y}\left(\mu \frac{\partial w}{\partial y}\right) \tag{A10}$$

The infinite-span swept-wing assumption implies

$$\frac{\partial}{\partial z}(\ ) = 0 \tag{A11}$$

and the continuity equation under the same assumption yields,

$$\rho v = -\int_0^y \frac{\partial}{\partial x}(\rho u)\,dy \tag{A12}$$

Along the locus of minimum velocity in the wake $\frac{\partial w}{\partial y} = 0$. Substituting (A11) and (A12) into (A10) and integrating with respect to y in the wake from 0 to δ_z, the following form of momentum integral equation in the wake can be derived.

$$\frac{d}{dx}\left[\rho_e u_e w_e \int_0^{\delta_z} \frac{\rho u}{\rho_e u_e}\left(1 - \frac{w}{w_e}\right)dy\right] = 0$$

$$\frac{d}{dx}\left[\rho_e u_e w_e\, \Theta_{uw}\right] = 0$$

$$\Theta_{uw_\infty} = \left(\frac{\rho_{e_{T.E.}}}{\rho_\infty}\right)\left(\frac{u_{e_{T.E.}}}{u_\infty}\right)\left(\frac{w_{e_{T.E.}}}{w_\infty}\right)(\Theta_{uw})_{T.E.} \tag{A13}$$

Thus, $C_{D_{wake}}$ can be written from equations (A4), (A9), and (A13) as:

$$C_{D_{wake}} = \frac{2}{c}\left[(\Theta_{uu})_{T.E.}\left(\frac{\rho_e}{\rho_\infty}\right)_{T.E.}\left(\frac{u_e}{u_\infty}\right)^p \cos^2\Lambda_{T.E.}\right.$$

$$\left. + (\Theta_{uw})_{T.E.}\left(\frac{\rho_e}{\rho_\infty}\right)_{T.E.}\left(\frac{w_{e_{T.E.}}}{w_\infty}\right)\sin^2\Lambda_{T.E.}\right] \tag{A14}$$

Equation (A14) contain terms evaluated at the trailing edge, such as $(\Theta_{uw})_{T.E.}$, $(\Theta_{uu})_{T.E.}$, $(\rho_e)_{T.E.}$, and $(u_e)_{T.E.}$. These values are computed in the framework of computer programs for boundary-layer methods, (refs. 5, 6, 7, and 8) and pressure-distribution prediction methods such as those of references 9 and 10.

202

REFERENCES

1. Harvey, William D.; Harris, Charles D.,; Brooks, Cyler W., Jr., Bobbitt Percy, J.; and Stack, John P.: Design and Experimental Evaluation of Swept Supercritical LFC Airfoil. NASA CP-2398, Vol. I, Langley Symposium on Aerodynamics, April 23-25, 1985.

2. Bobbitt, P. J.; Waggoner, E. G.; Harvey, W. D.; and Dagenhart, J. R.: A Faster "Transition" to Laminar Flow. SAE Paper 851855, October 14-17, 1985.

3. Meyer, R. R.; and Jennett, L. A.: In Flight Surface Oil Flow Photographs with Comparison to Pressure Distribution on Boundary-Layer Data. NASA TP 2393, April 1985.

4. Meyer, R. R.; Trujillo, B. M.; and Bartlett, D. W.: F-14 VSTEF and Results of the Cleanup Flight Test Program. NLF and LFC Research Symposium, NASA Langley Research Center, March 16-19, 1987.

5. Goradia, Suresh H.; and Morgan, Harry L.: Theoretical Methods and Design Studies for NLF and HLFC Swept Wings at Subsonic and Transonic Speeds. Natural Laminar Flow and Laminar Flow Control Symposium, NASA Langley Research Center, Hampton, VA, March 16-19, 1987.

6. Goradia, S. H.; Bobbitt, P. J.; Ferris, J. C.; and Harvey, W. D.: Theoretical Investigations and Correlative Studies for NLF, HLFC, and LFC Swept Wings at Subsonic, Transonic and Supersonic Speeds. SAE Technical Paper 871861, presented at the Aerospace Technology Conference and Exposition, Long Beach, CA, October 5-8, 1987.

7. Goradia, S. H.; Bobbitt, P. J.; and Ferris, J. C.: Correlative and Design Studies for NLF and HLFC Swept Wings at Subcritical and Supercritical Mach Numbers. Paper presented at the 1986 SAE Aerospace Technology Conference and Exposition, Long Beach, CA, October 13-16, 1986.

8. Goradia, S. H.; and Morgan H. L.: A New, Improved Method for Separating Turbulent Boundary Layer for Aerodynamic Performance Prediction of Trailing-Edge Stall Airfoils. Paper presented at AIAA 4th Applied Aero-dynamics Conference, June 9-11, 1986, San Diego, CA.

9. Bauer, F.; Garabedian, P.; and Korn, D.: A Theory of Supercritical Wing Sections with Computer Programs and Examples, Vol. 66, Lecture Notes in Economics and Mathematical Systems, Springer-Verlag, 1972.

10. Stevens, W. A.; Goradia, S.; and Braden, J. A.: Mathematical Model for Two-Dimensional Multi-Component Airfoils in Viscous Flow. NASA CR-1843, 1971.

$M_\infty \sin \Lambda$

M_∞

$M_\infty \cos \Lambda$

$u(s,\xi)$ — Velocity profile in streamwise direction

$v(s,\xi)$ — Velocity profile in direction normal to wall

$w(s,\xi)$ — Velocity profile in spanwise direction
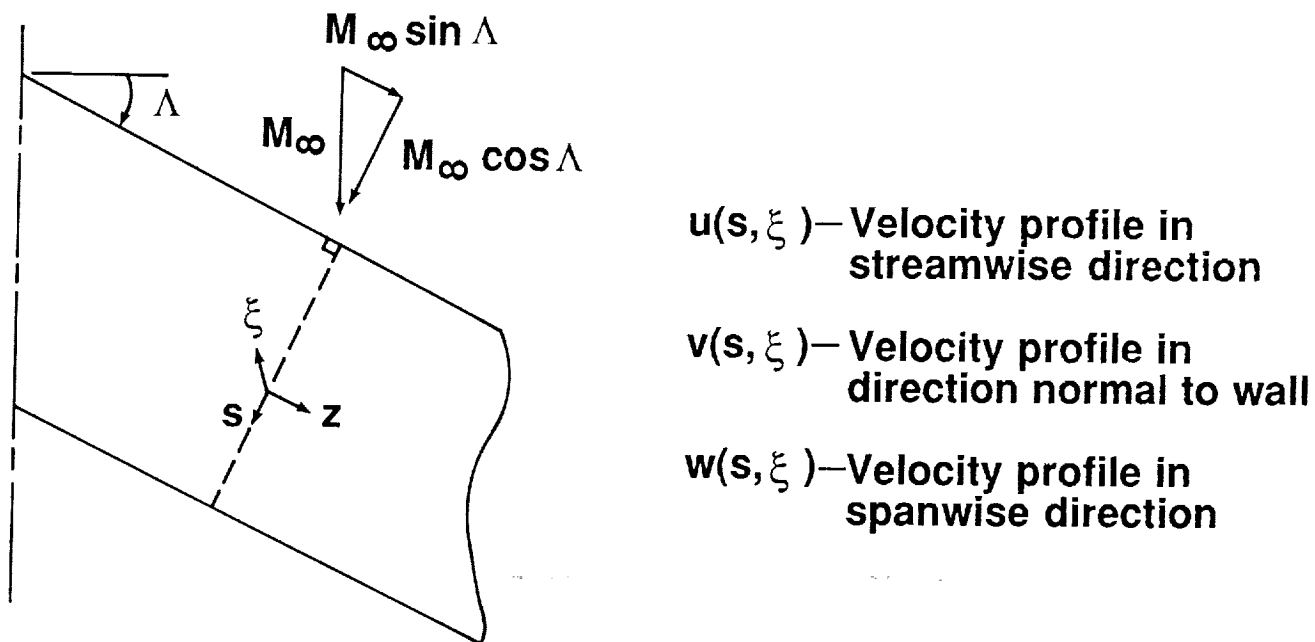
Figure 1. - Definition of coordinate axis system.

Control volume

Forward-swept wing
(Finite, tapered, & twisted)

u - Boundary layer velocity in s direction
v - Boundary layer velocity in ξ direction
w - Boundary layer velocity in z direction

Δz

P, pressure

Δs

$P + \dfrac{dP}{dz}\Delta z$

p

$A_1 B_1 C_1 D_1$ - Wing surface

A,B,C,D - Edge of boundary layer

F_z - Algebraic sum of forces in z directions
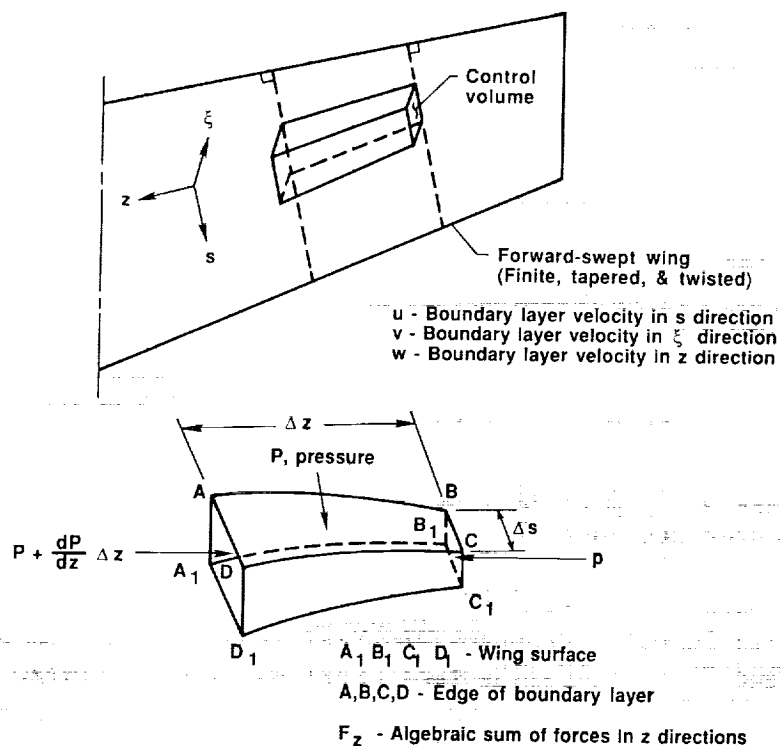
Figure 2. - Schematic of control volume used to account for boundary-layer wash-in/wash-out phenomena.

$$\frac{a_o M_e \theta_{P,n}}{v_m(1+.2M_e^2)^2}$$

Neutral

Unstable

Stable

$$v_m = \frac{1}{\delta_{P,n}} \int_0^{\delta_{P,n}} v\, d\xi$$

$$n = s \text{ or } z$$

$$\frac{a_o \theta_{P,n}}{\alpha v_m} \left(\frac{dM_e}{d\eta}\right)\frac{1}{(1+.2M_e^2)^2}$$
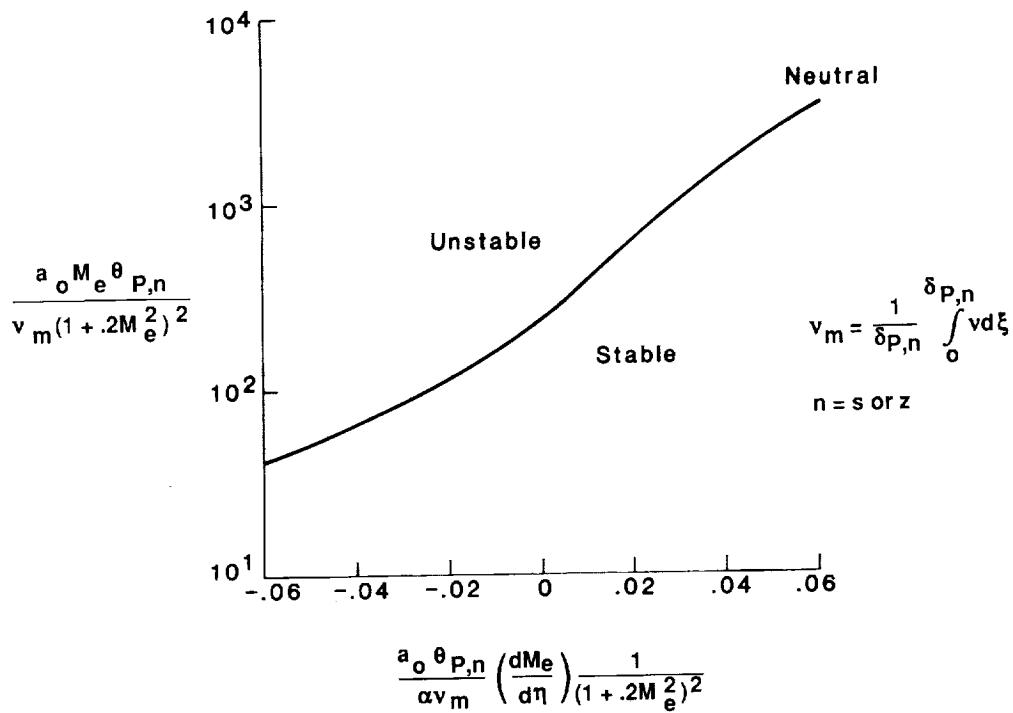
Figure 3. - Criteria for determining laminar boundary-layer neutral instability.

$$\chi = \frac{\int_{\zeta_{inst}}^{\zeta} \delta_{T,n}^{**} \left(\frac{T_o}{T_e}\right)^{-6} \frac{a_o}{\alpha} \frac{dM_e}{d\zeta}\, d\zeta}{\int_{\zeta_{inst}}^{\zeta} v_m \alpha \left(\frac{T_o}{T_e}\right)^{-4} d\eta}, \text{ where } \zeta = s \text{ or } z$$

$R_{tran} - R_{inst}$

.04

.2

.5

1

Free-stream turbulence 2%

χ
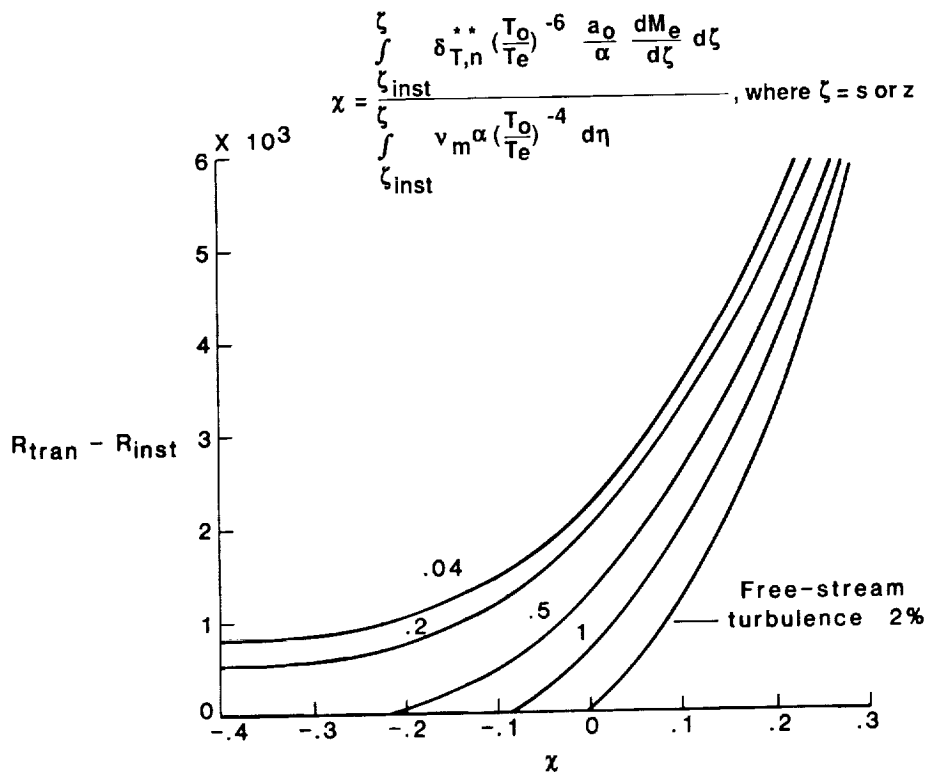
Figure 4. - Criteria for determining laminar boundary-layer transition.

205

$$R_{T,n} = \frac{\left(\begin{smallmatrix}U_e \\ \text{or} \\ W_e\end{smallmatrix}\right)\delta_{T,n}^{**}}{\nu_m} \quad \text{and} \quad \delta_{T,n}^{**} = \int_0^\infty \left[1 - \left\{\begin{smallmatrix}\frac{U}{U_e} \\ \text{or} \\ \frac{W}{W_e}\end{smallmatrix}\right\} \frac{T_e}{T} \, d\zeta\right]$$

where $\zeta = s$ or z

Data of Vandrist, Boison, Deem, Erickson,
Schubaur, Scramstad, Hall, Bishop, Dryden etc.
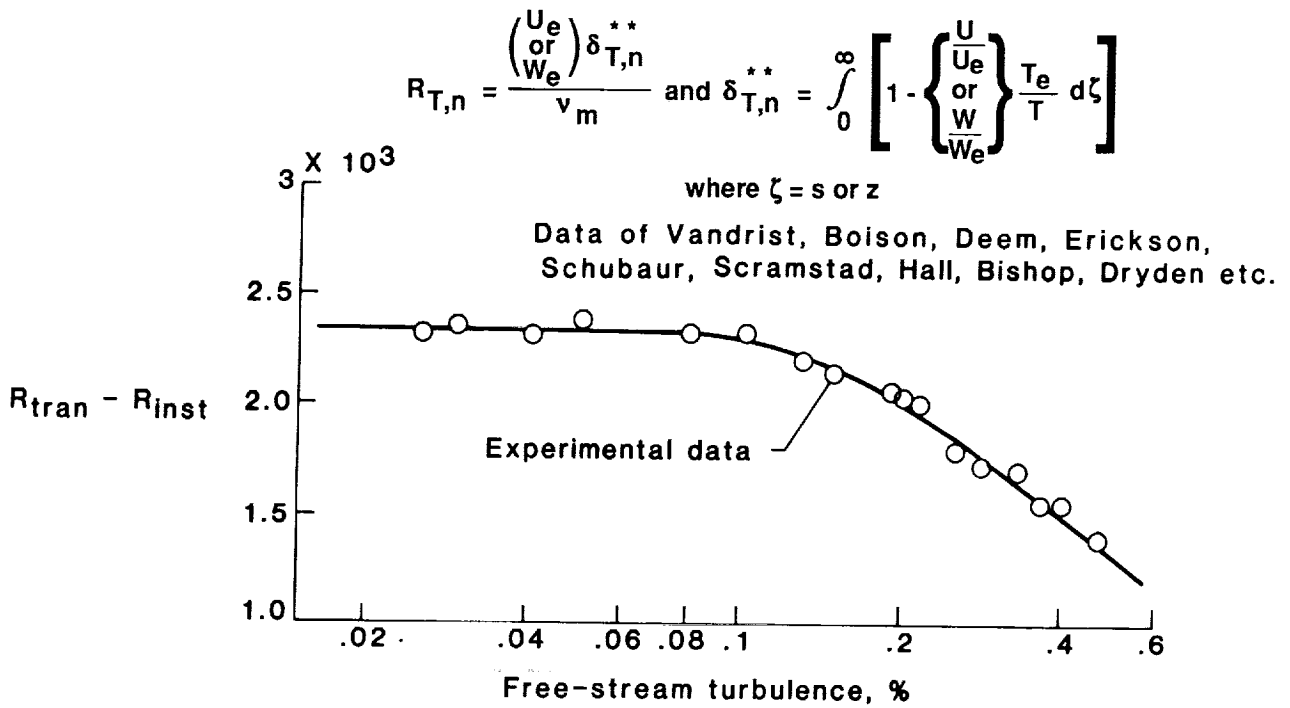
Figure 5. - Effect of free-stream turbulence on the difference of transition and instability Reynolds numbers.

- Three rows of flush static pressure orifices
- Three rows of surface pitot tubes
- Five hot-film gauges
- Two boundary-layer rakes
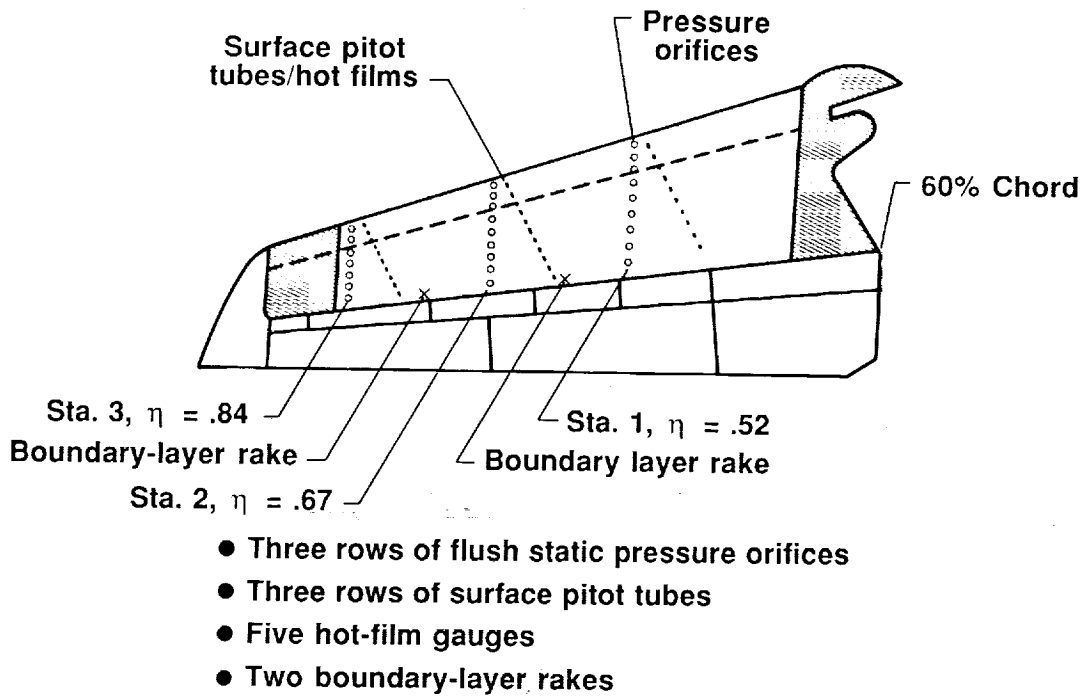
Figure 6. - Planform of an instrumentation on the gloved F-14 wing.
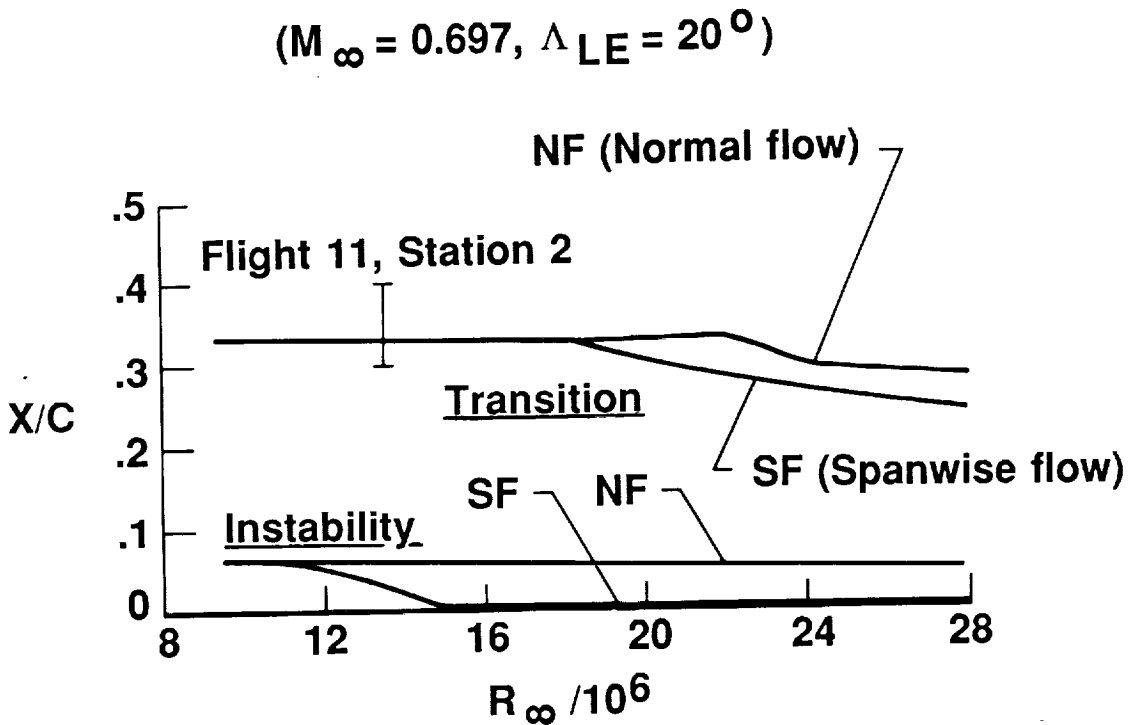
$(M_\infty = 0.700, \Lambda_{LE} = 20.0^\circ, R_\infty = 13 \times 10^6)$

$\eta = 0.52$ $\eta = 0.67$ $\eta = 0.84$

HOT FILM TRACES
Station 2

(a) Experimental pressure distributions and hot-film traces.

$(M_\infty = 0.697, \Lambda_{LE} = 20^\circ)$

(b) Computed transition locations as a function of free-stream chord Reynolds number.

Figure 7. - Results for the F-14 "clean-up" gloved wing for a leading- edge sweep of 20° and M_∞ of 0.7.

207

$(M_{\infty} = 0.697, \Lambda_{LE} = 20^{\circ}, R_{\infty} = 13.6 \times 10^{6})$
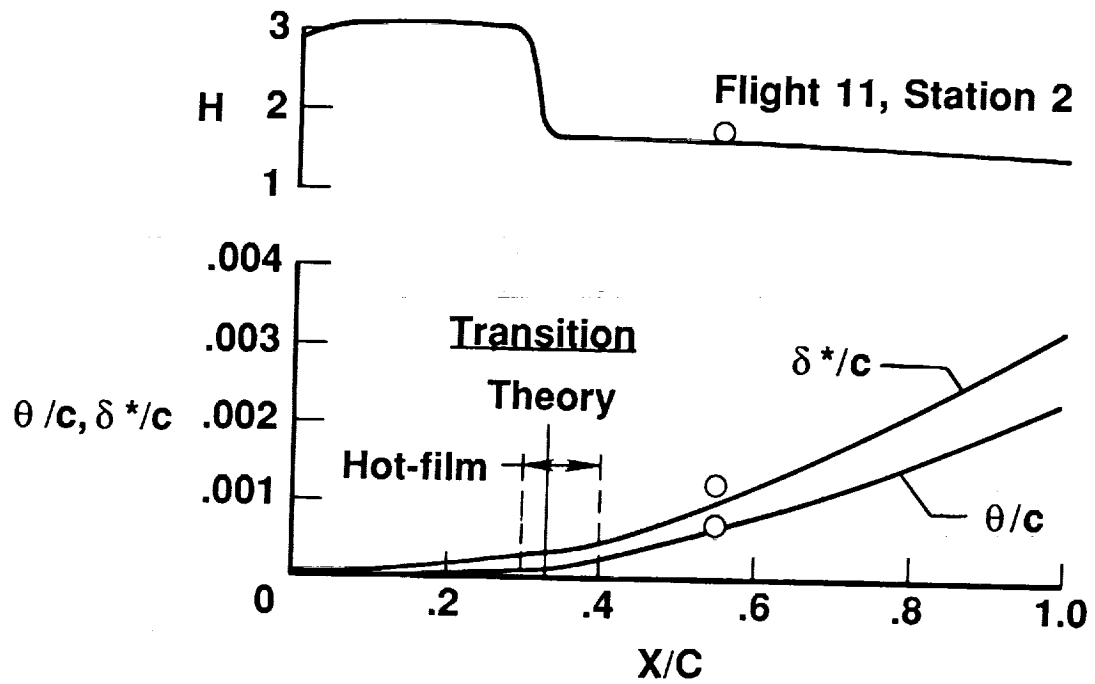
(c) Comparison between computed and flight boundary-layer parameters for $R_{\infty} = 13 \times 10^{6}$.

Figure 7. - Concluded.

η = 0.52   η = 0.67   η = 0.84
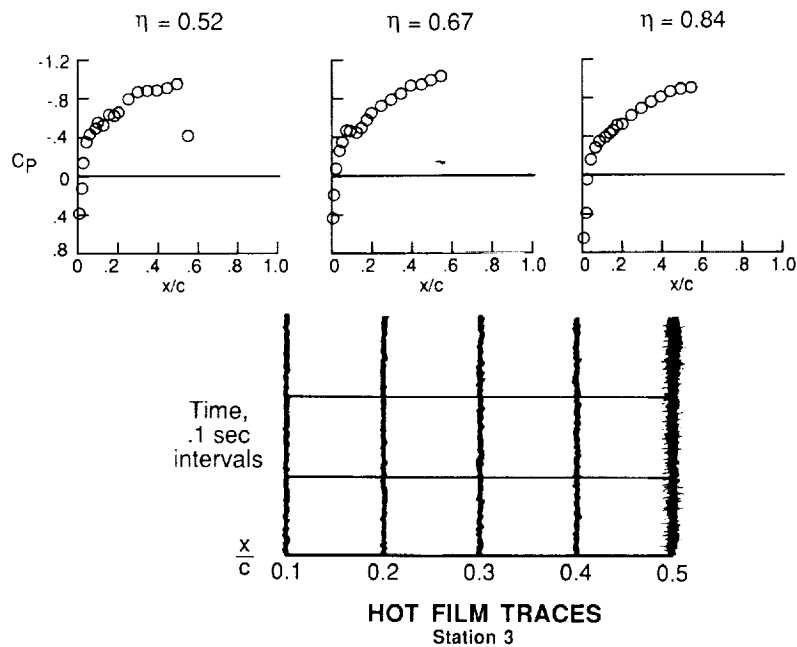
(a) Experimental pressure distributions and hot-film traces for $R_\infty = 11 \times 10^6$.

η = 0.52   η = 0.67   η = 0.84
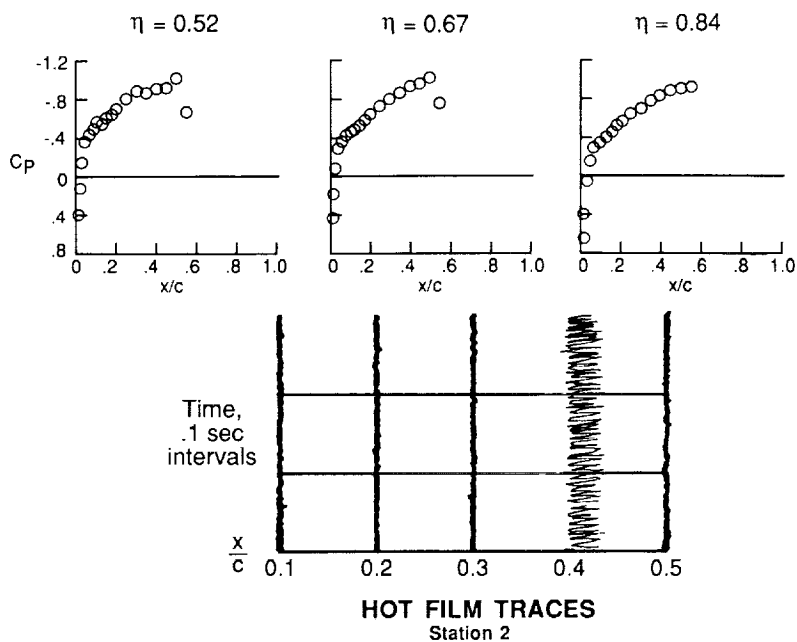
(b) Experimental pressure distributions and hot-film traces for $R_\infty = 23 \times 10^6$.

Figure 8. - Results for the F-14 "clean-up" gloved wing for a leading-edge sweep of 20° and M_∞ of 0.8.
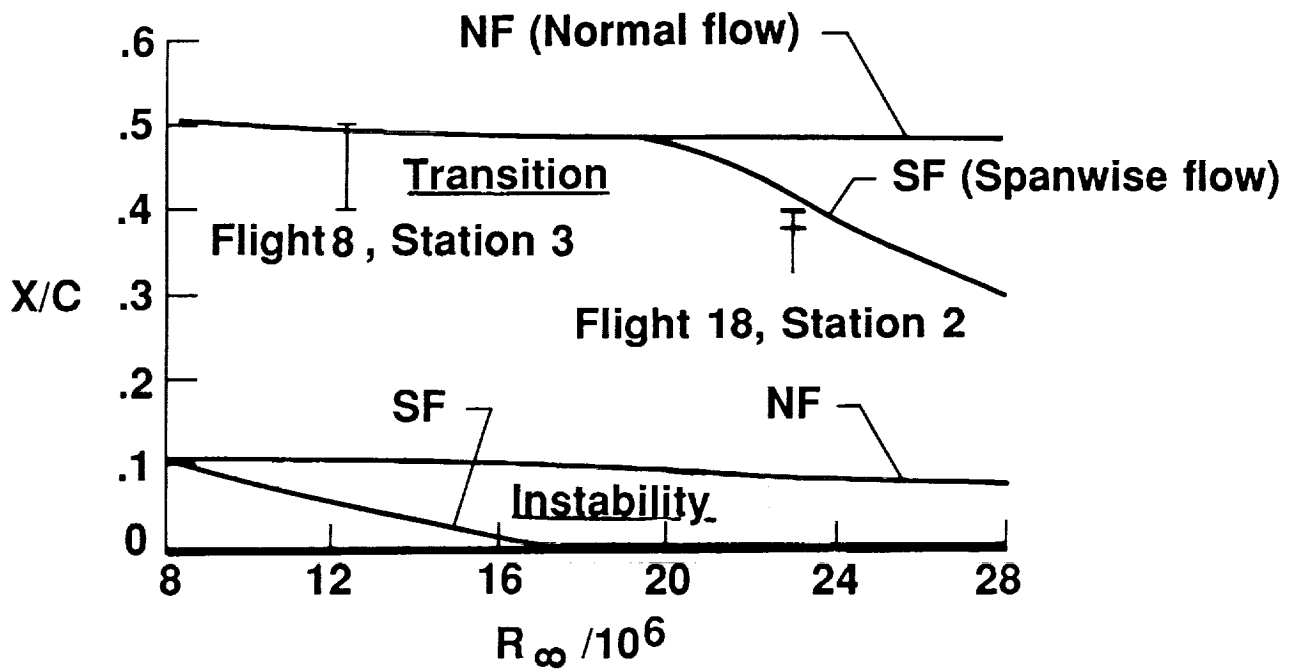
(c) Computed transition and instability locations versus free-stream Reynolds number.

$$(\Lambda_{LE} = 20^{\circ} \text{ , Station 3})$$
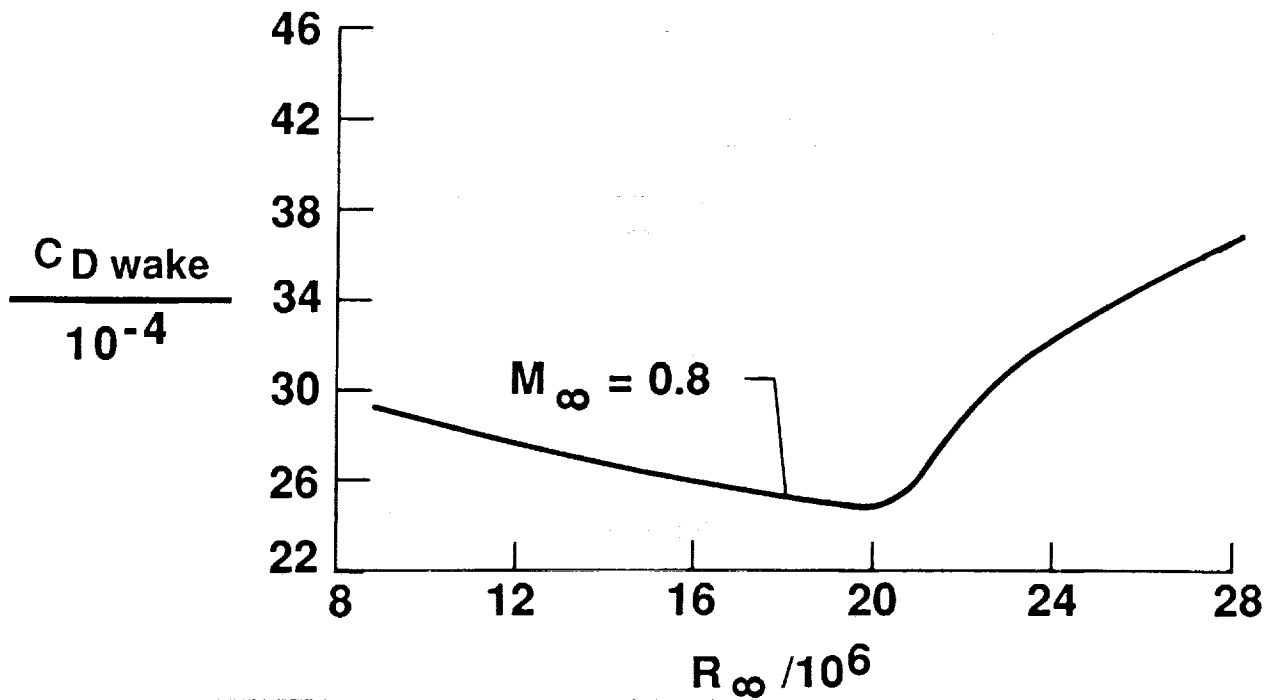
(d) Computed $C_{D_{wake}}$ versus free-stream chord Reynolds number.

Figure 8. - Continued.
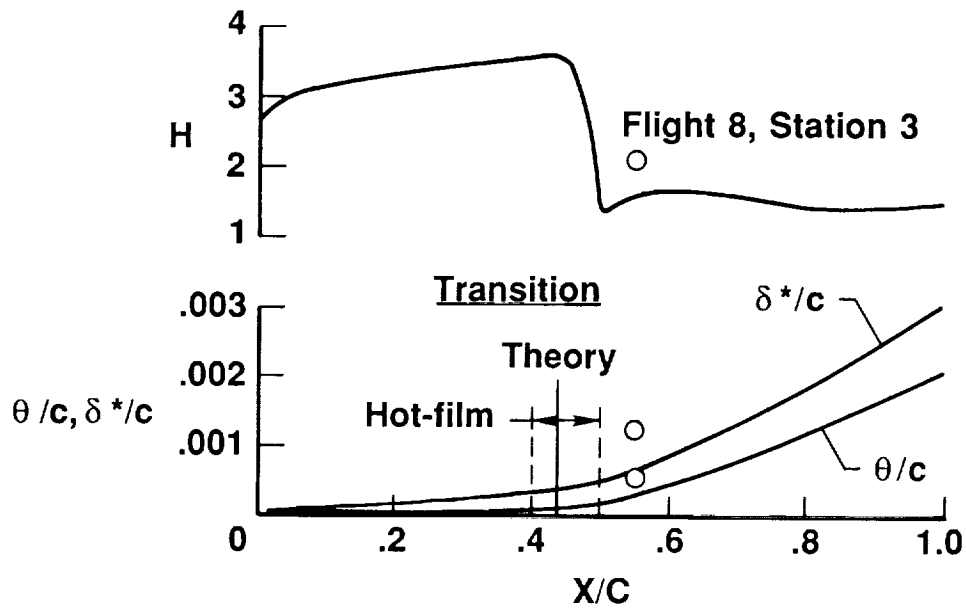
(e) Comparison between computed and flight boundary-layer parameters for $R_\infty = 12.4 \times 10^6$.

Figure 8. - Concluded.

$\eta = 0.52$ $\eta = 0.67$ $\eta = 0.84$

HOT FILM TRACES
Station 3
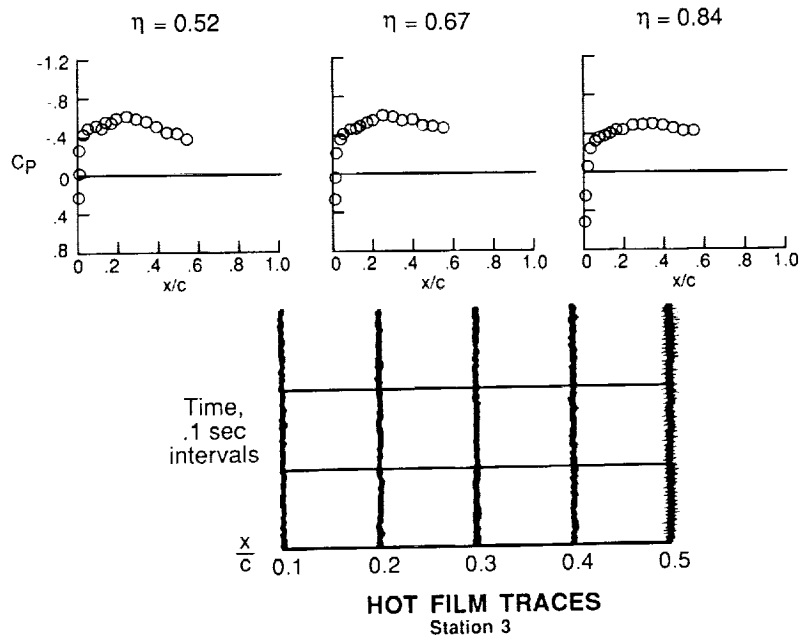
(a) Experimental pressure distributions and hot-film traces.

(b) Computed transition locations as a function of free-stream chord Reynolds number.

Figure 9. - Results for the F-14 "clean-up" gloved wing for a leading-edge sweep of 25° and M_∞ of 0.7.
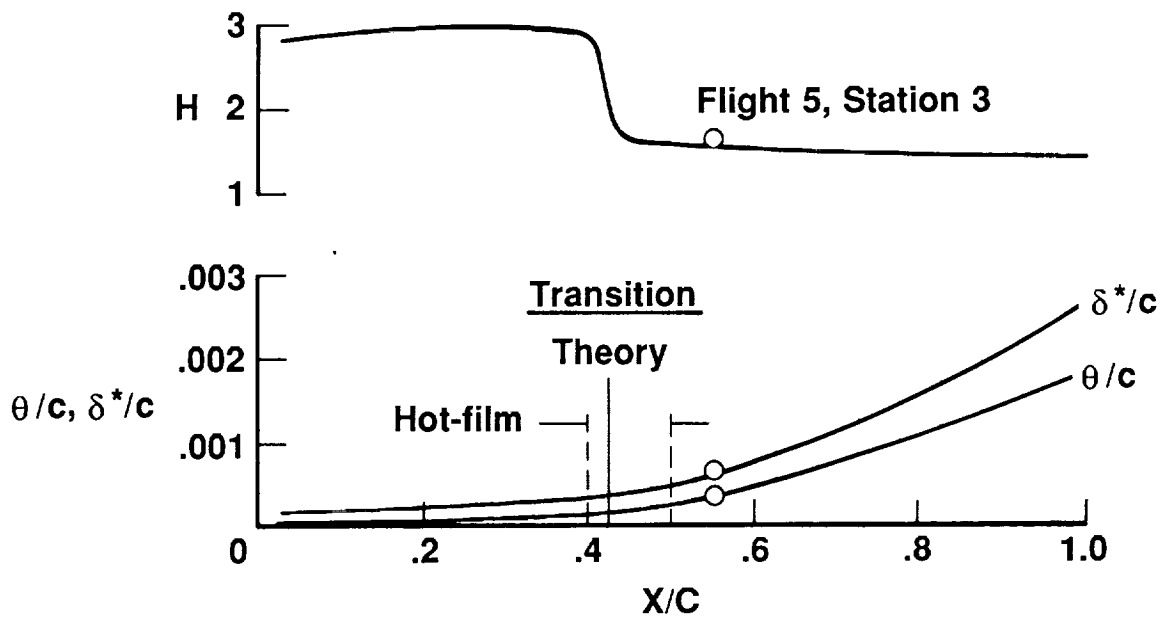
(c) Comparison between computed and flight boundary-layer parameters for $R_\infty = 10.8 \times 10^6$.

Figure 9. - Concluded.
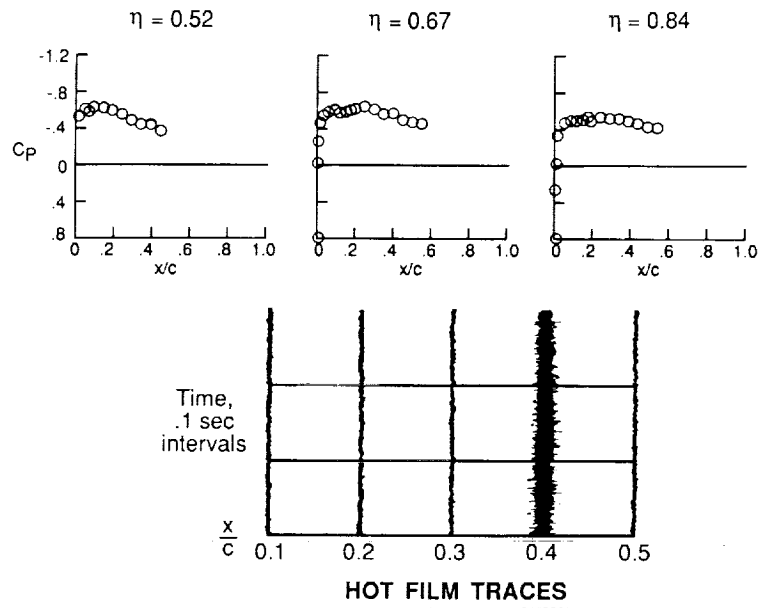
(a) Experimental pressure distributions and hot-film traces for $R_\infty = 9.5 \times 10^6$.
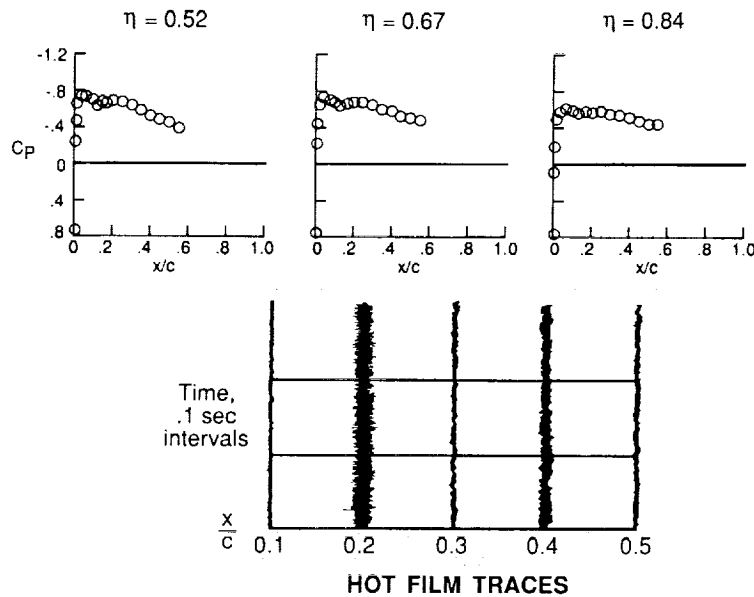
(b) Experimental pressure distributions and hot-film traces for $R_\infty = 19.2 \times 10^6$.

Figure 10. - Results for the F-14 "clean-up" gloved wing for a leading-edge sweep of 30° and M_∞ of 0.7.
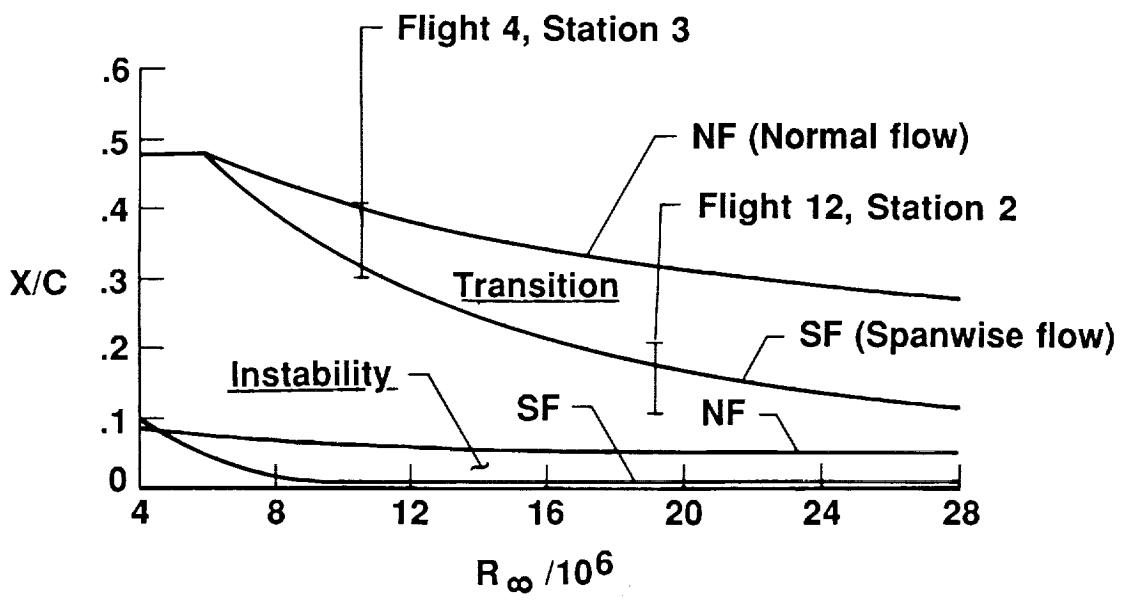
(c) Computed transition and instability locations versus free-stream Reynolds number.

Figure 10. - Concluded.
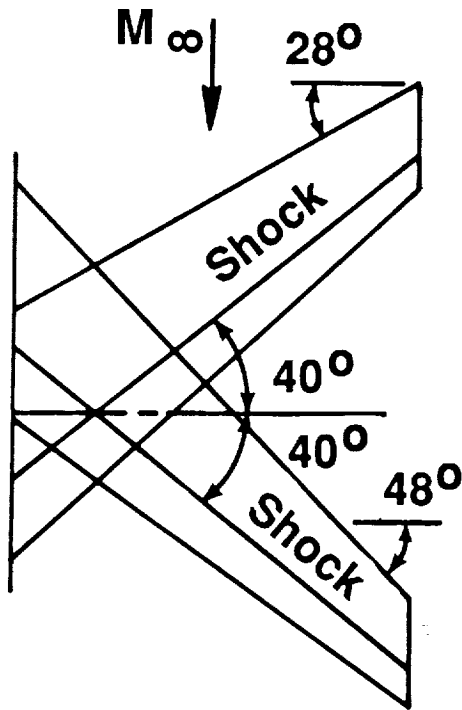
(a) Planforms.

(AR = .4, Taper ratio = .4)
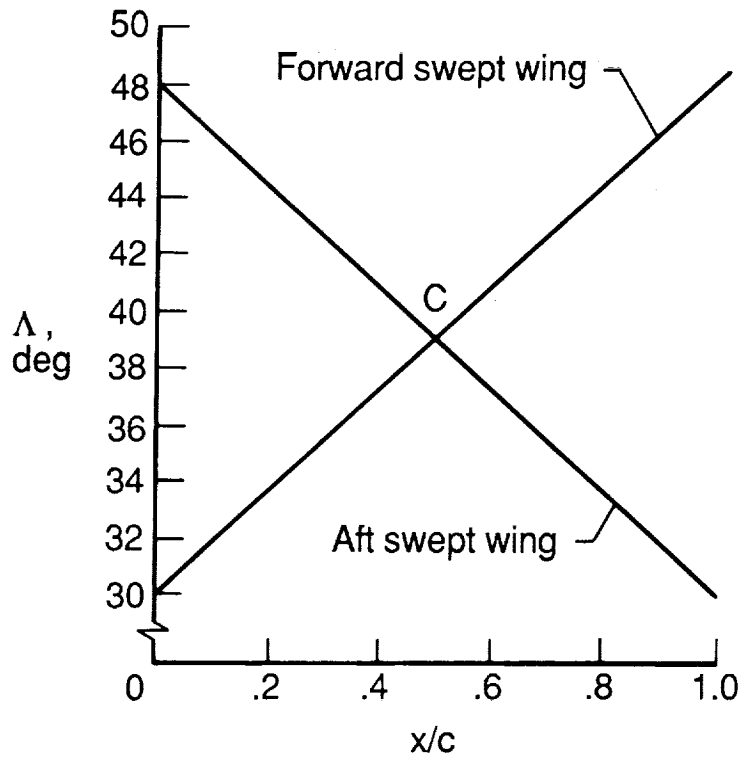
(b) Local sweep variations with respect to x/c.

Figure 11. - Comparison between "equivalent" forward and aft swept wings.
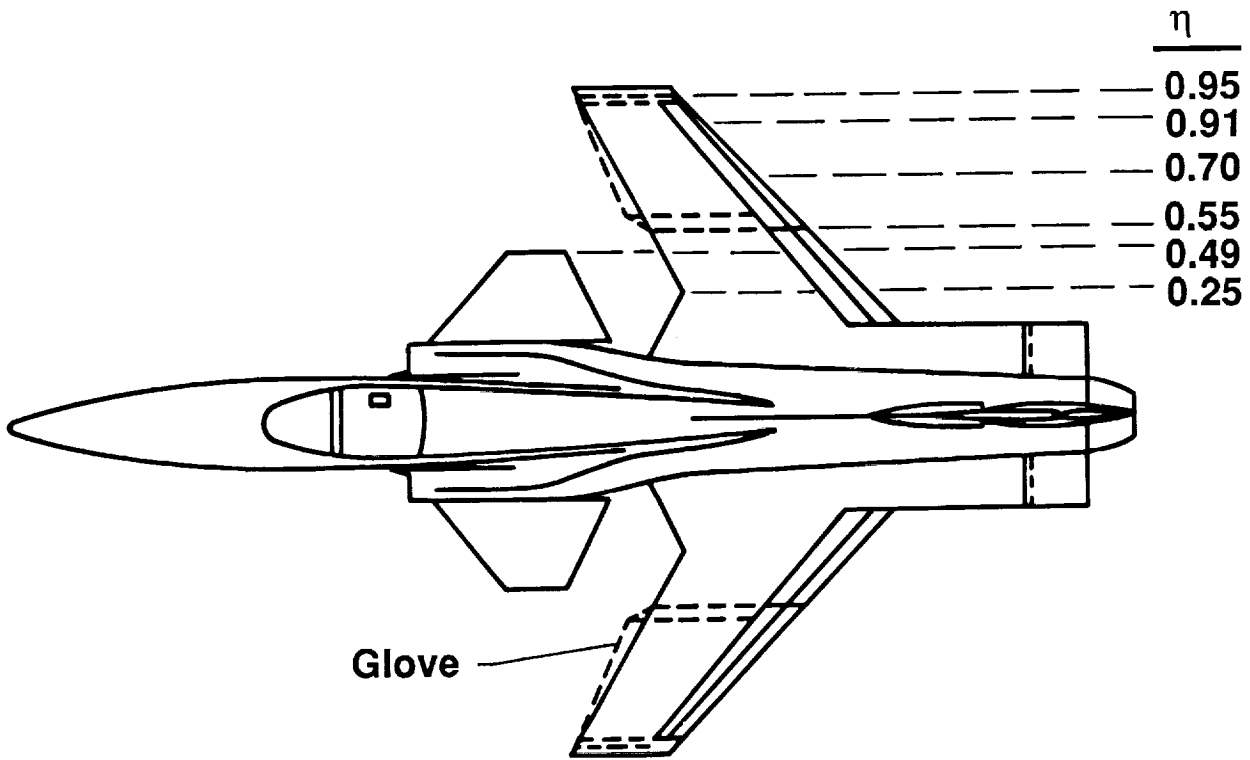
Figure 12. - Planform of X-29 aircraft.
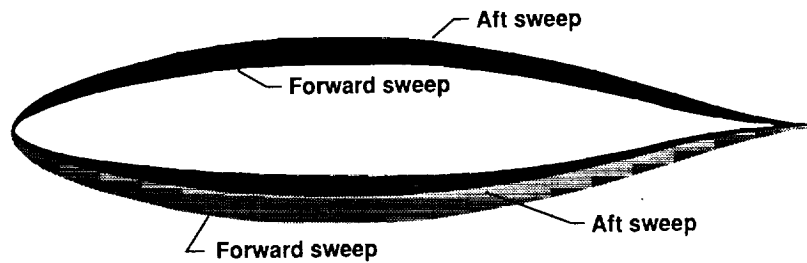
$(Z/C)_N = (Z/C)_S /cos \Lambda$ upper and lower for Aft Sweep (N = normal, S = streamwise)

$(Z/C)_{N,upper} = (Z/C)_{S,upper}$
$\left.\rule{0pt}{26pt}\right\}$ Forward Sweep
$(Z/C)_{N,lower} = (Z/C)_{S,upper} \cdot [1/cos\Lambda -1] + (Z/C)_{S,lower} \cdot [1/cos \Lambda]$

$(M_L)_N = (M_L)_S \cdot cos \Lambda_{X/C=0.25}$
$\left.\rule{0pt}{26pt}\right\}$ Forward and Aft Sweep
$(C_P)_{streamwise} = (C_P)_N \cdot cos^2 \Lambda$ where $\Lambda = \Lambda_{LE} + (\Lambda_{TE} - \Lambda_{LE}) \cdot (X/C)$

$(C_L)_{2-D} = (C_L)_S /cos^2 \Lambda_{X/C=0.25}$

Figure 13. - Sweep procedure for forward- and aft-swept wings.

217
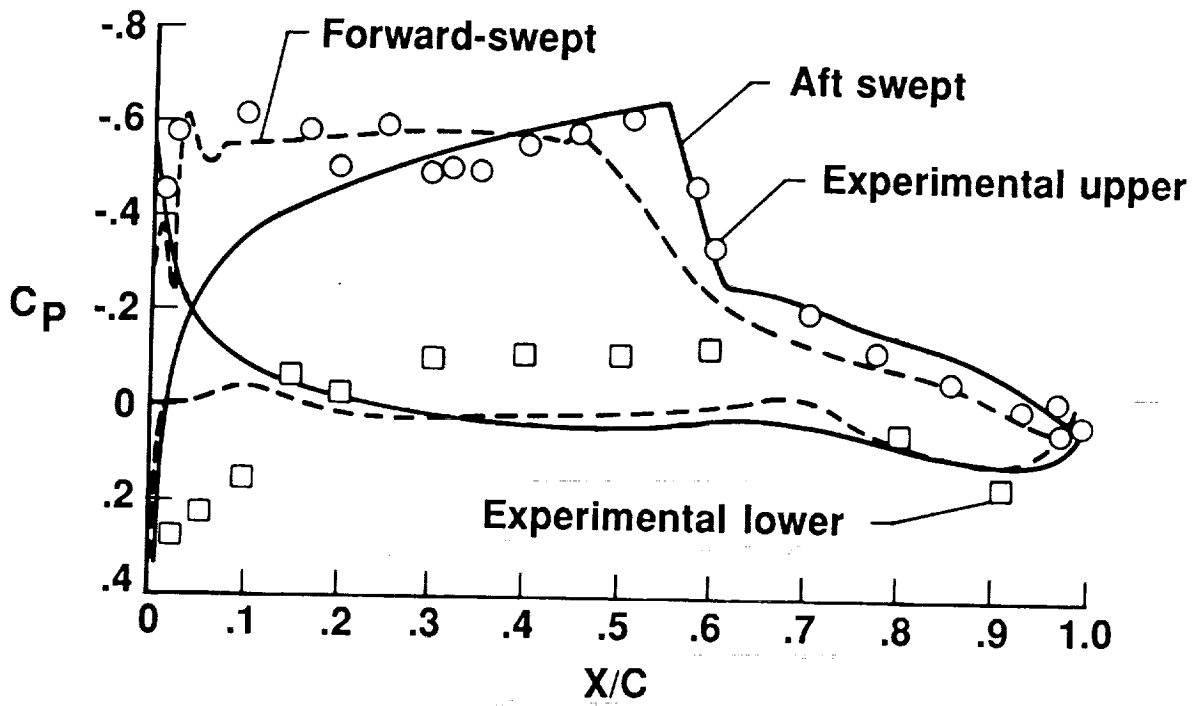
Figure 14. - Computational results for the pressure distributions on the X-29 wing section situated on both forward and aft wings. (M_∞ = 0.91, η = 0.70, Λ_{LE} = 30°)
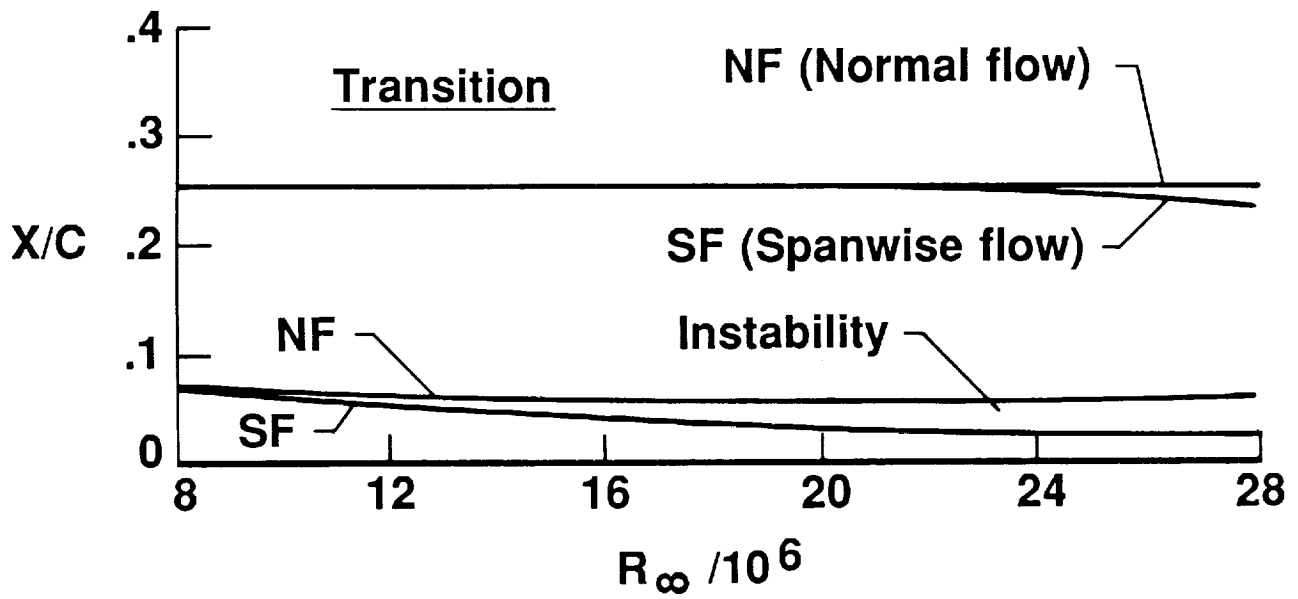
(a) Transition location versus R_∞.
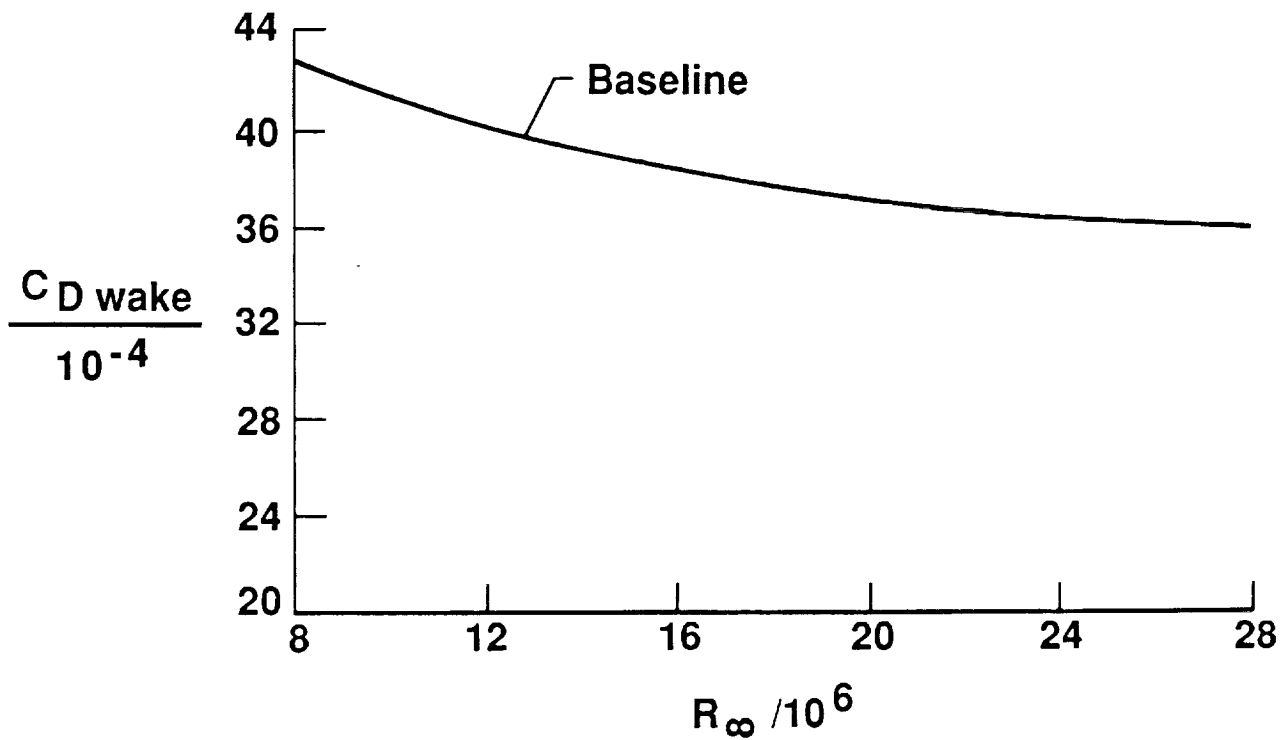
(b) $C_{D_{wake}}$ for baseline versus R_∞ and comparison with NLF-Glove.

Figure 15. - Computed results for X-29 baseline section for η = 0.7, M_∞ = 0.91.

Λ LE = 30°
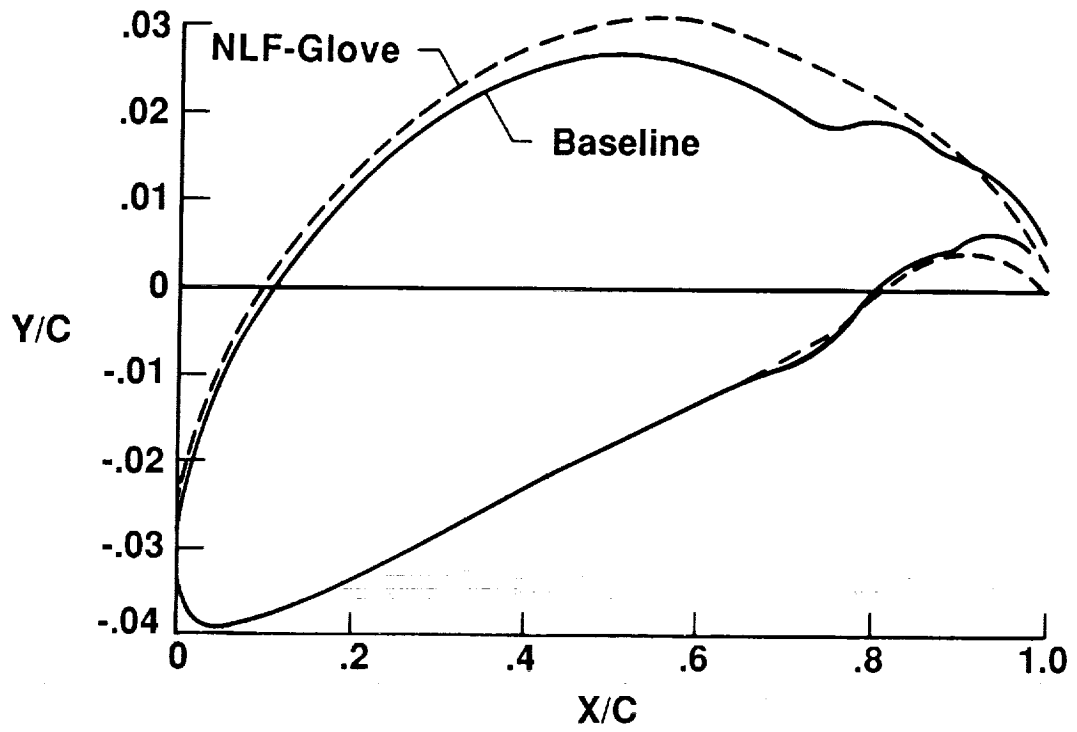
Figure 16. - Comparison between baseline geometry and NLF-Glove for X-29 wing for η = 0.7.
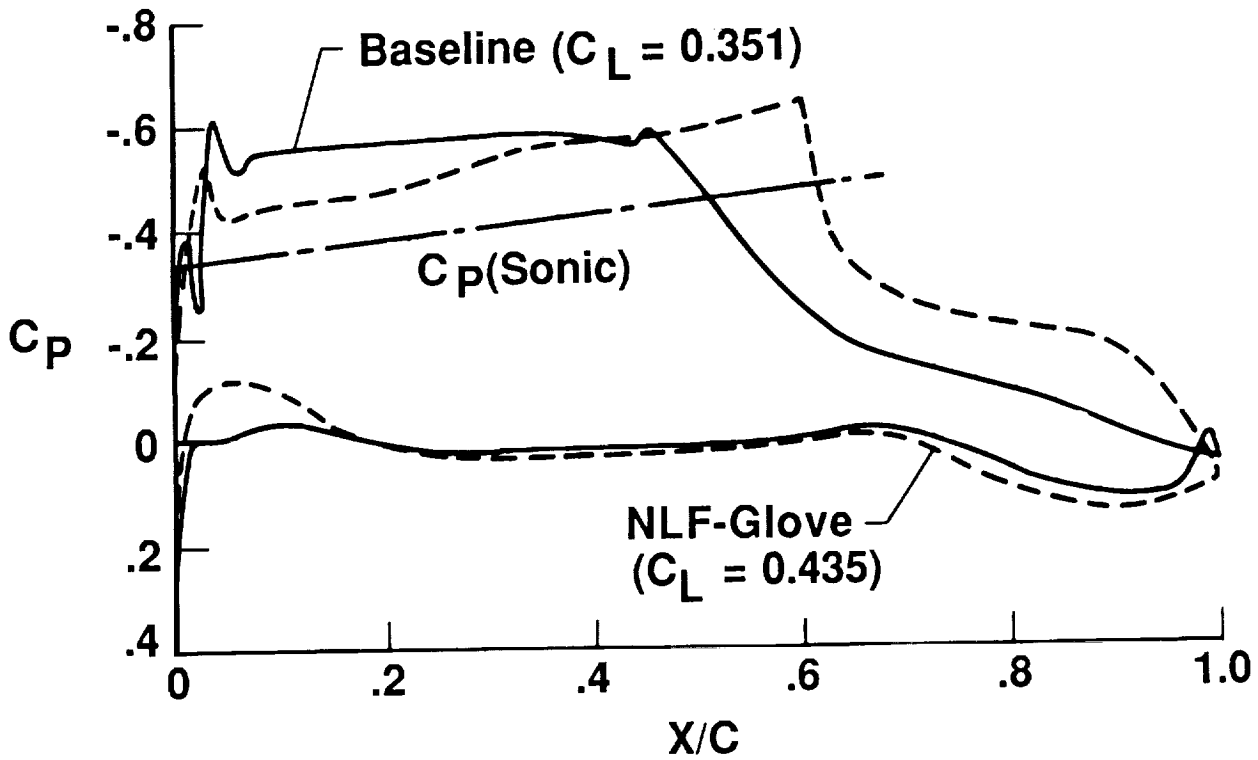
(a) Comparison between baseline and NLF-Glove for M_∞ = 0.905 and leading-edge sweep of 30°.
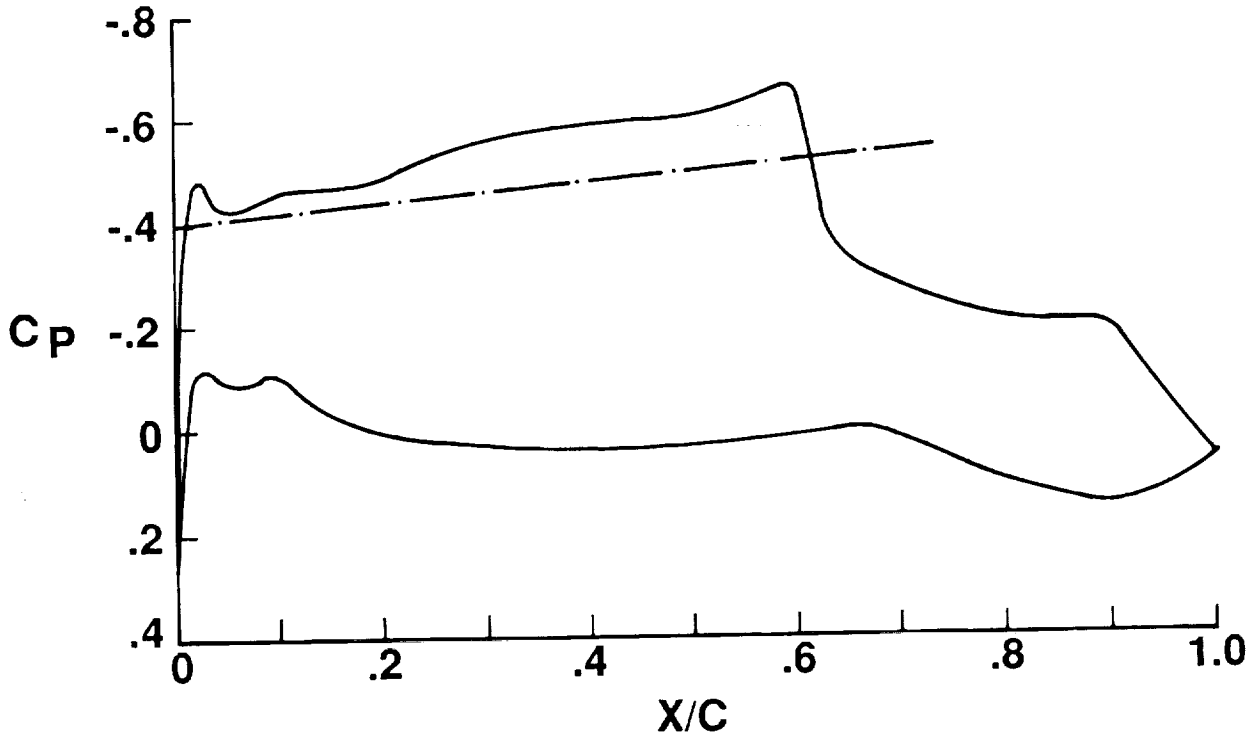
(b) Pressure distribution for M_∞ = 0.865 and leading-edge sweep of 25°.

Figure 17. - Chordwise pressure distributions for X-29 wing section for η = 0.7 and transition location computations.
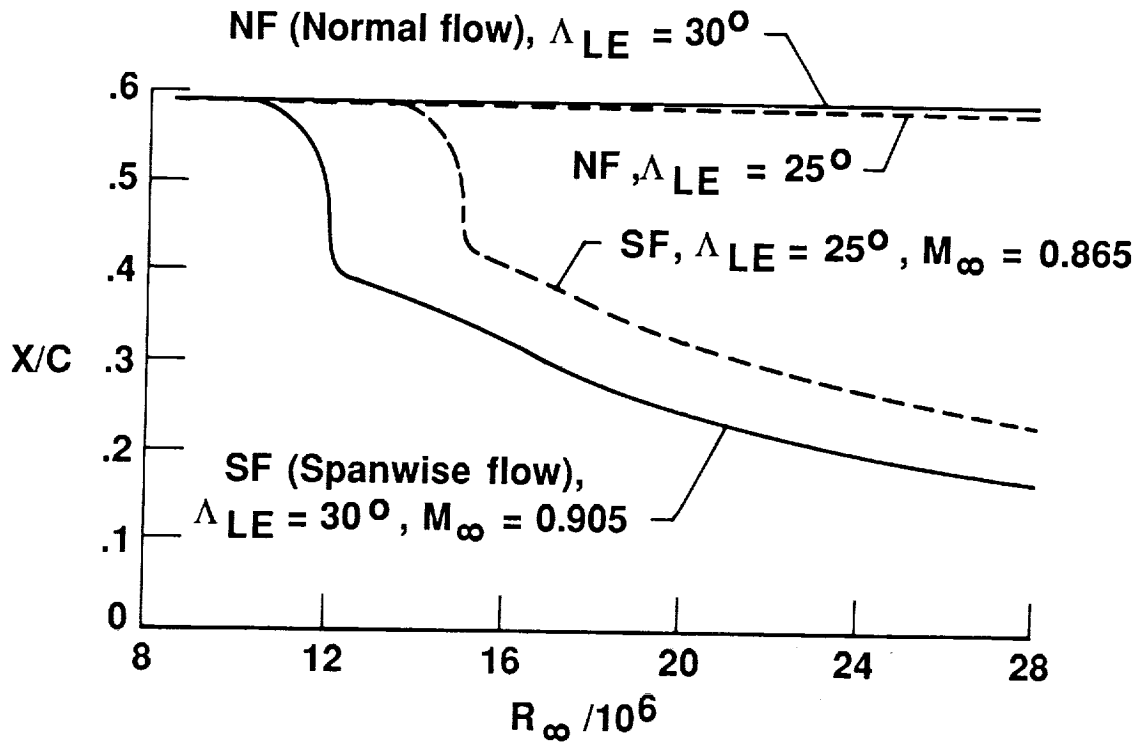
(c) Transition characteristics for leading-edge sweeps of 30° and 25°.
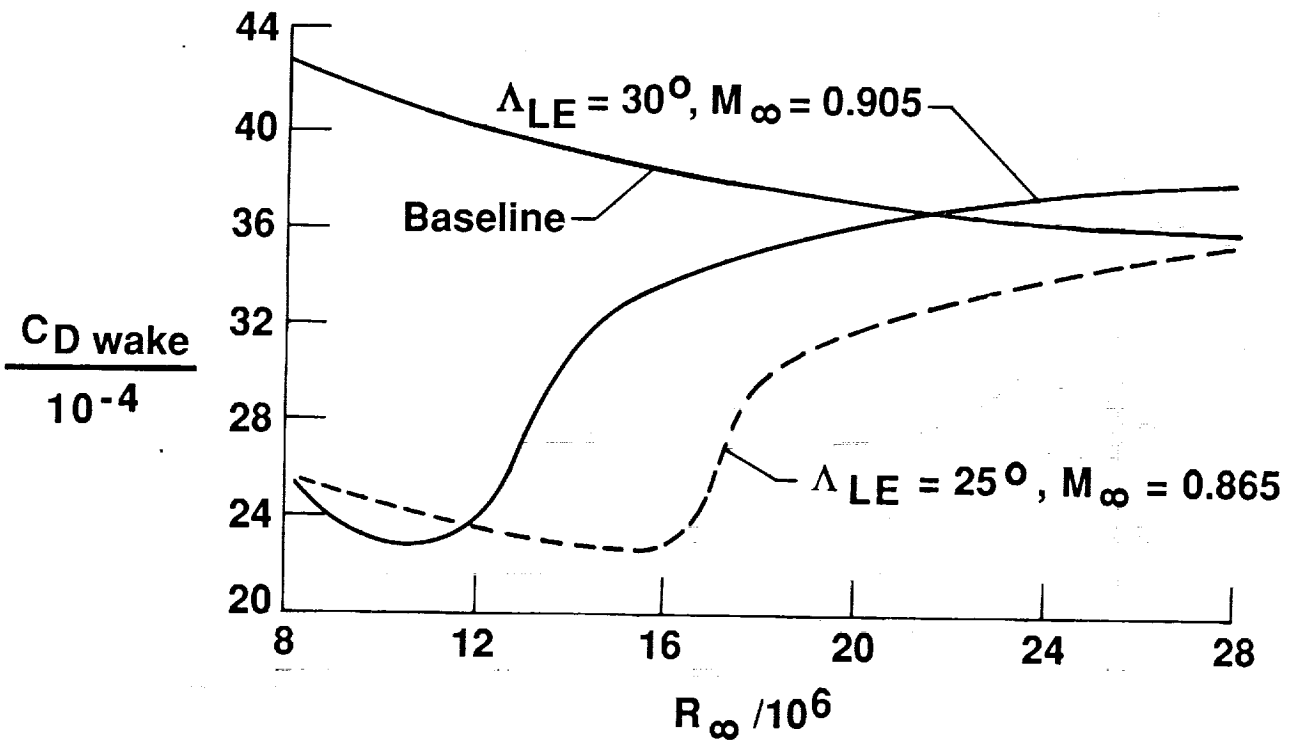
(d) Effect of Reynolds number and leading-edge sweep on $C_{D_{wake}}$.

Figure 17. - Concluded.
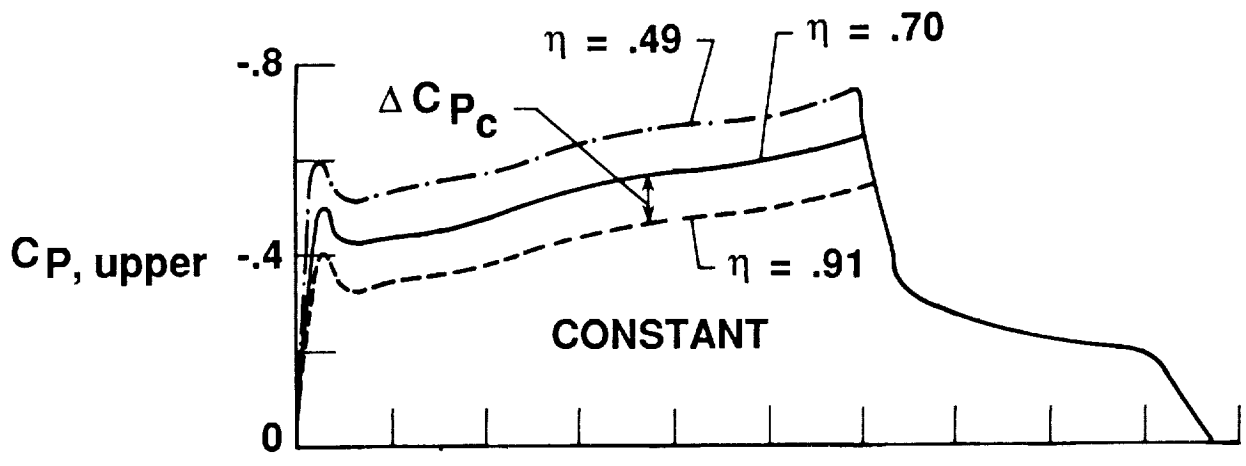
(a) Constant spanwise pressure gradient.
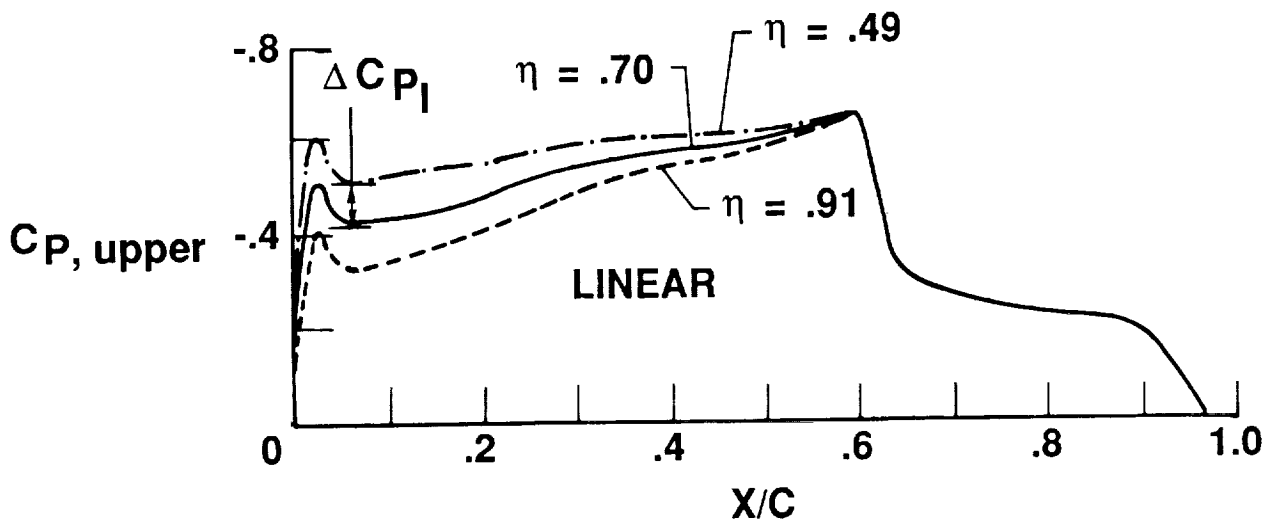
(b) Linearly varying spanwise pressure gradient.

Figure 18. - Schematics showing types of spanwise pressure gradients studied.

$(M_\infty = 0.905,\ \Lambda_{LE} = 30^{\circ})$

NF, $\Delta C_{P_C} = .15$

NF (Normal flow), $\Delta C_{P_C} = 0$

SF, $\Delta C_{P_C} = .15$

SF (Spanwise flow), $\Delta C_{P_C} = 0$

X/C

$R_\infty / 10^6$
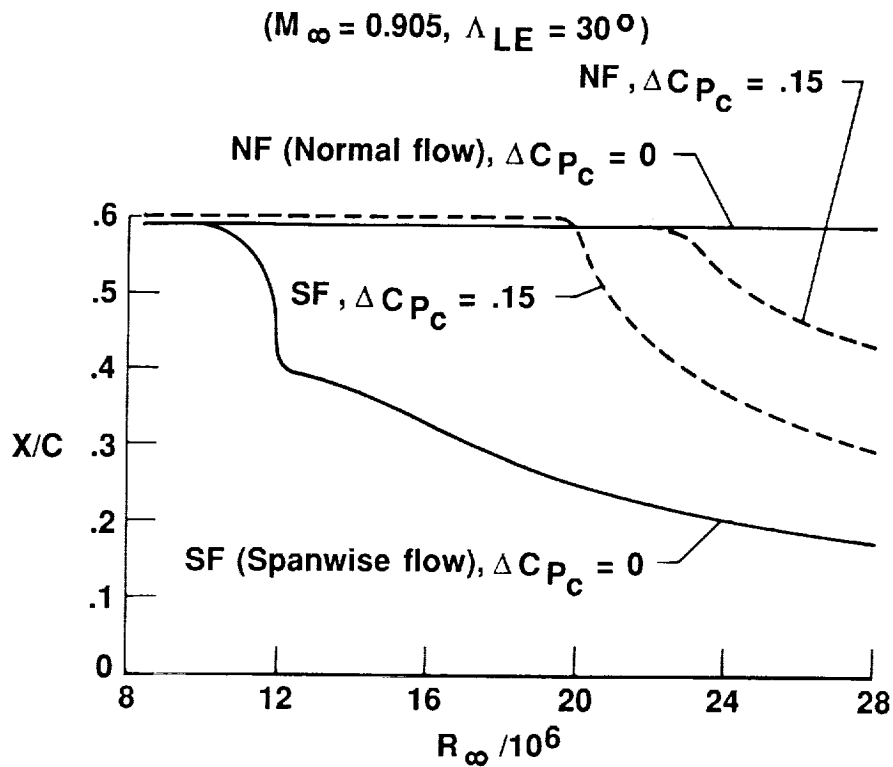
Figure 19. - Comparison of the effect of a constant spanwise pressure gradient of $\Delta C_{P_C} = 0.15$ on transition with that for zero spanwise gradient, i.e., with $\Delta C_{P_C} = 0$.

$(M_\infty = 0.905,\ \Lambda_{LE} = 30^{\circ})$

$\Delta C_{P_C} = 0$

.05

.10

.15

$\dfrac{C_{D\ wake}}{10^{-4}}$

$R_\infty / 10^6$
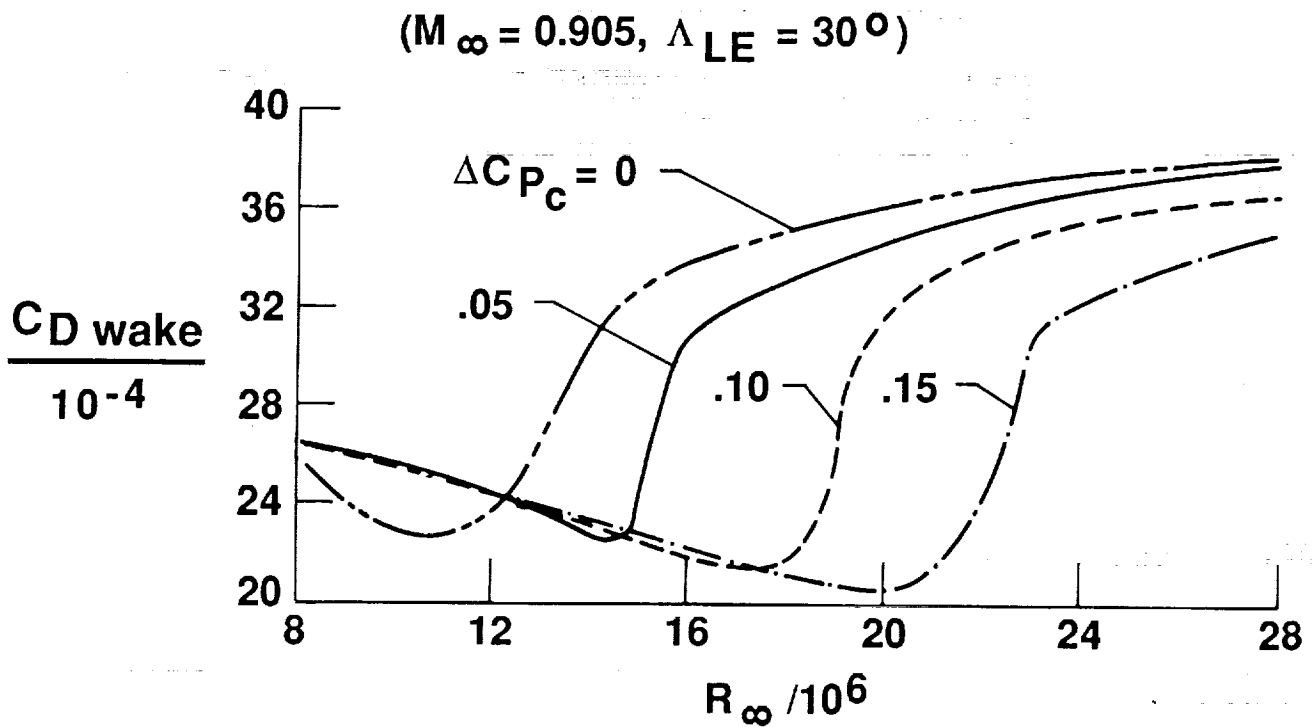
Figure 20. - $C_{D_{wake}}$ versus R_∞ with ΔC_{P_C} as parameter for X-29 glove.

(M $_\infty$ = 0.905, Λ_{LE} = 30°)
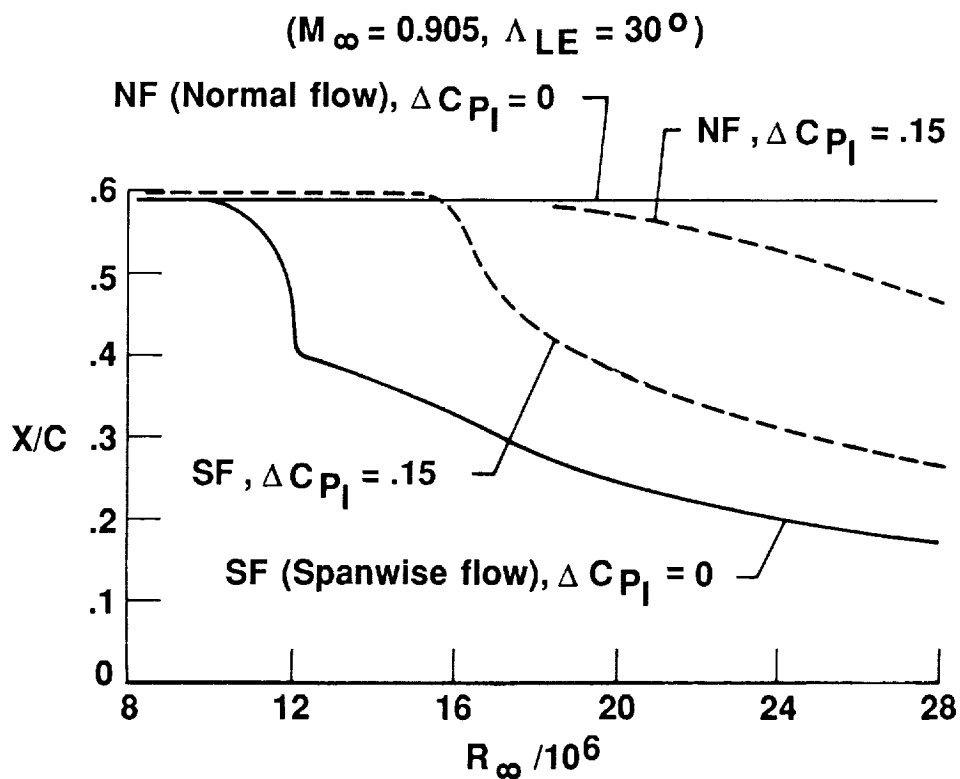
Figure 21. - Effect of linear spanwise pressure gradient of ΔC_{P_1} = 0.15 on transition characteristics of X-29 glove and comparison with ΔC_{P_1} = 0.
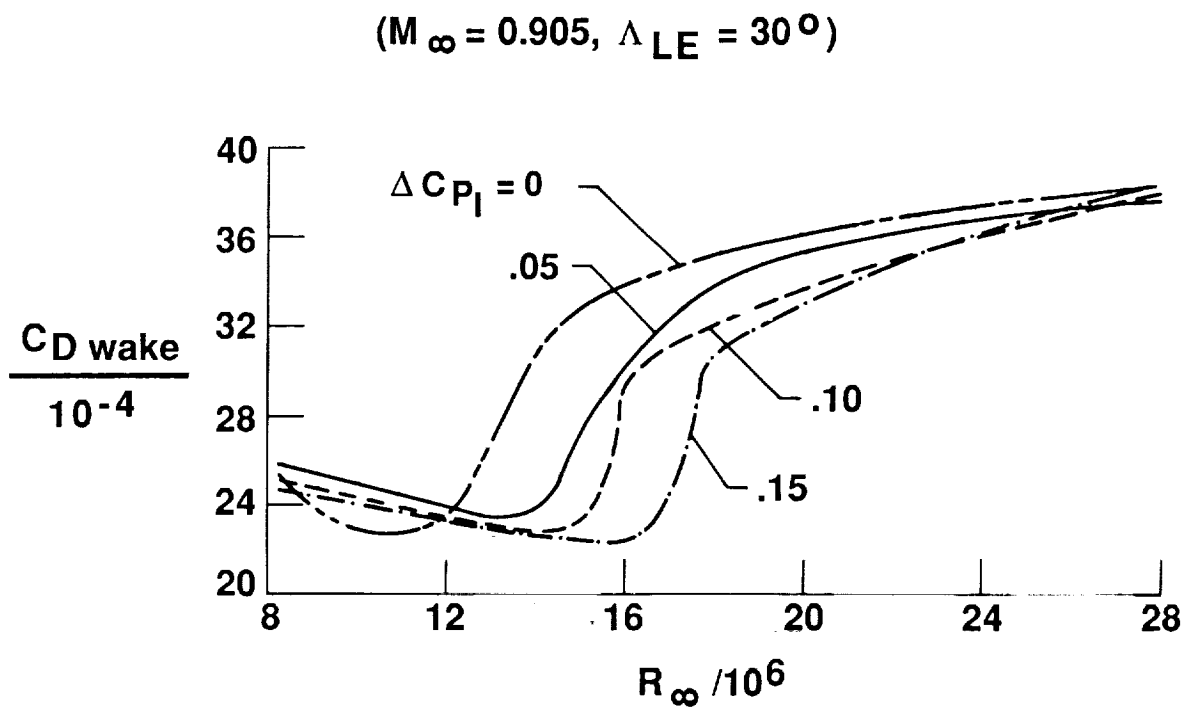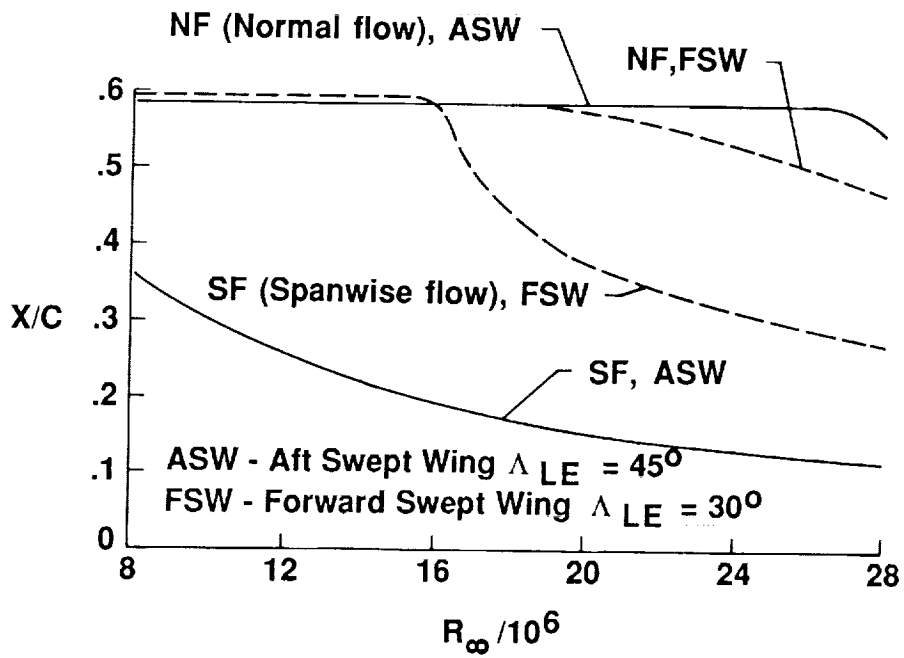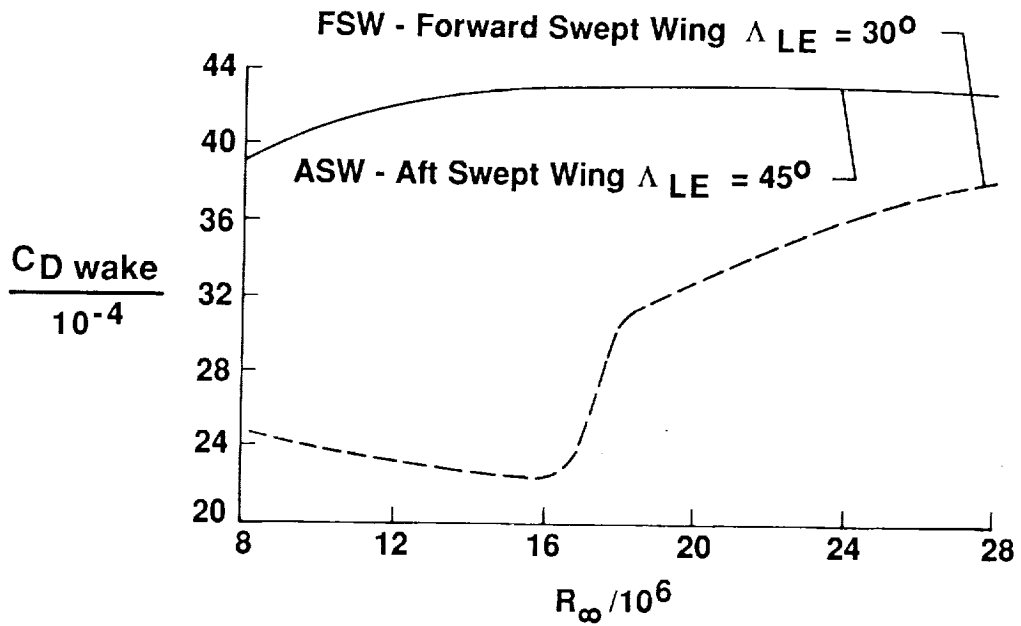
(M $_\infty$ = 0.905, Λ_{LE} = 30°)

Figure 22. - $C_{D_{wake}}$ versus R_∞ with ΔC_{P_1} as parameter for X-29 glove.
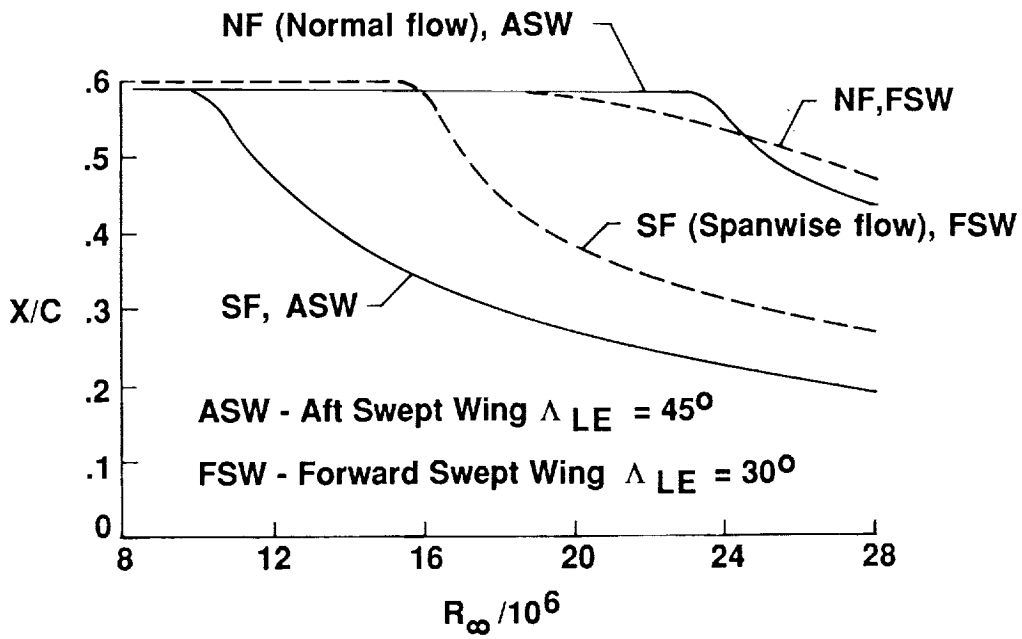
(a) Transition Location versus R_∞ for $\Delta C_{p_1} = 0.15$.
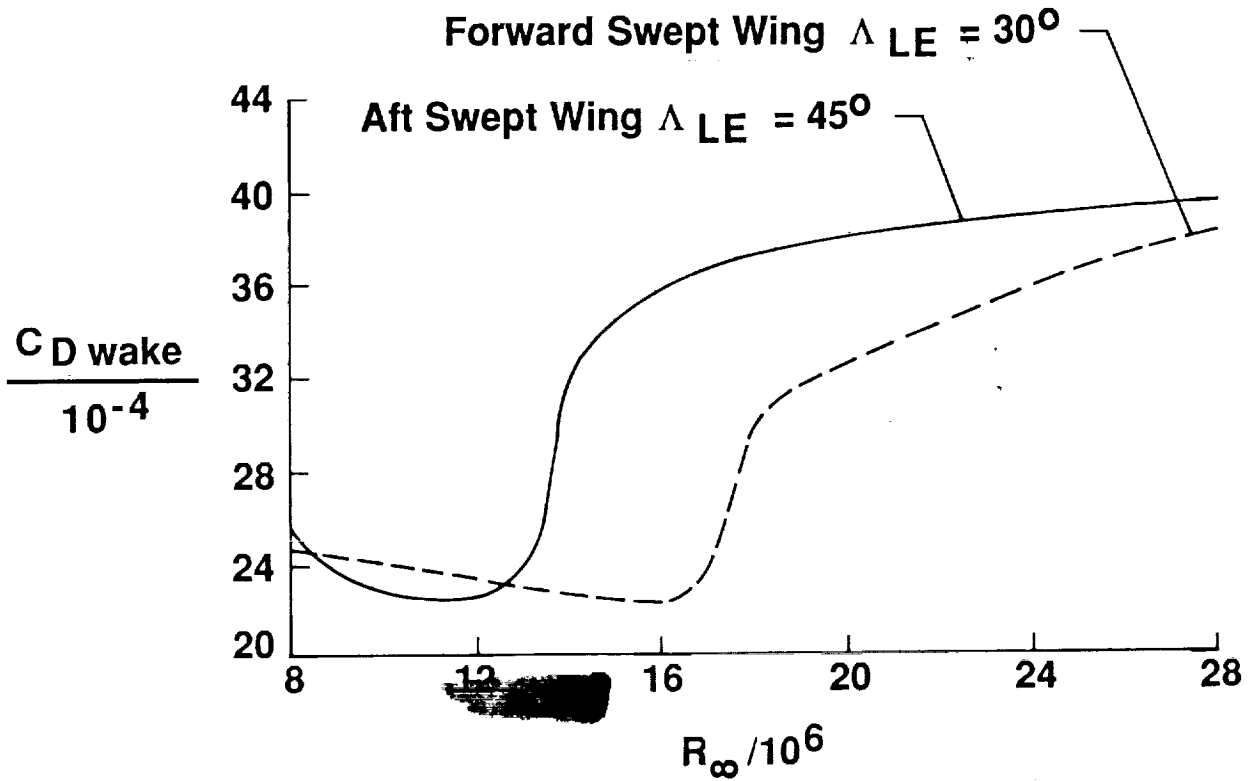

(b) $C_{D_{wake}}$ versus R_∞ for $\Delta C_{p_1} = 0.15$.

Figure 23. - Comparison between FSW and "equivalent" ASW for $M_\infty = 0.905$ and $C_L = 0.435$.

(c) Transition location versus R_∞ for $\Delta C_{P_1} = -0.15$.

(d) $C_{D_{wake}}$ versus R_∞ for $\Delta C_{P_1} = -0.15$.

Figure 23. - Concluded.